Inorganic Chemistry

Article

pubs.acs.org/IC

Trigonal Pyramidal $\{AsO_2(OH)\}$ Bridging Tetranuclear Rare-Earth Encapsulated Polyoxotungstate Aggregates

Hailou Li,[†] Yajie Liu,[†] Rui Zheng,[†] Lijuan Chen,*[,†] Jun-Wei Zhao,*[,†] and Guo-Yu Yang*[,‡]

[†]Henan Key Laboratory of Polyoxometalate Chemistry, Institute of Molecule and Crystal Engineering, College of Chemistry and Chemical Engineering, Henan University, Kaifeng, Henan 475004, People's Republic of China

[‡]MOE Key Laboratory of Cluster Science, School of Chemistry, Beijing Institute of Technology, Beijing 100081, People's Republic of China

Supporting Information

ABSTRACT: The one-pot assembly reaction of $Na_2WO_4{\cdot}2H_2O$, $RE(NO_3)_3{\cdot}6H_2O$, and $NaAsO_2$ in the participation of dimethylamine hydrochloride as an organic solubilizing agent in the acidic aqueous solution led to a class of trigonal pyramidal $\{AsO_2(OH)\}$ bridging rare-earth substituted arsenotungstate (AT) aggregates $[H_2N(CH_3)_2]_8Na_8\{[W_3RE_2(H_2O)_8AsO_8(OH)][B\text{-}\alpha\text{-}AsW_9O_{33}]_2\}_2{\cdot}65H_2O$ [RE = Eu^{III} (**1**), Gd^{III} (**2**), Tb^{III} (**3**), Dy^{III} (**4**), Ho^{III} (**5**), Y^{III} (**6**)], which were structurally characterized by elemental analyses, IR spectra, single-crystal X-ray diffraction, and thermogravimetric (TG) analyses. The common structural feature of **1**−**6** is that their polyoxoanions consist of a novel tetrameric unit $[(W_3RE_2(H_2O)_8AsO_8(OH))(B\text{-}\alpha\text{-}AsW_9O_{33})_2]_2^{16-}$ constituted by four trivacant Keggin $[\alpha\text{-}AsW_9O_{33}]^{9-}$ fragments linked through an unseen elliptical $[W_6RE_4(H_2O)_{16}As_2O_{16}(OH)_2]^{20+}$ moiety. Their polyoxoanionic infrastructures can also be described as a fusion of two equivalent dimeric subunits $[(W_3RE_2(H_2O)_8O_7)(B\text{-}\alpha\text{-}AsW_9O_{33})_2]^{8-}$ bridged via two μ_2-$\{AsO_2(OH)\}$ linkers. To the best of our knowledge, such a linking mode with trigonal pyramidal $\{AsO_2(OH)\}$ groups as linkers connecting adjacent RE containing polyoxometalate moieties together is very rare. The thermal stability of **1**−**6** was also investigated on the crystalline samples, and the thermal decomposition processes of **1**, **4**, and **6** were comparatively deeply studied. The fluorescent properties and decay times of **1**, **3**, and **4** were measured, and they exhibit the characteristic emissions of RE centers. The lifetimes of **1** and **3** mainly originate from the contribution of RE ions whereas the overall lifetime of **4** is contributed by the synergistic interactions of AT fragments and Dy^{3+} ions.

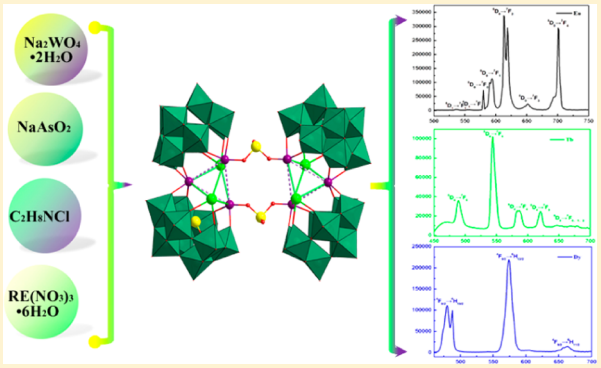

INTRODUCTION

Polyoxometalates (POMs), as an excellent class of anionic metal−oxygen clusters, have attracted a high level of attention not only on account of their structural diversities that are composed of metal centered $\{MO_n\}$ polyhedra linked by sharing corners, edges, or faces but also by reasons such as their potential applications in catalysis, magnetism, medicine, electronic materials, and nonlinear optics.[1] Among them, arsenotungstates (ATs) as an important subfamily bear enormous diversity of structures and properties and have attracted increasing interest throughout the past several decades. Moreover, the metal functionalization of ATs by transition-metal (TM) or rare-earth (RE) ingredients to construct novel TM or RE containing ATs has become an important and hot research topic. To date, a large number of TM containing ATs with fascinating structures and properties have been extensively discovered.[2−5] Furthermore, great developments on RE containing ATs (RECATs) have also been made due to the flexible and versatile combination between AT segments and RE linkers. As early as 1997, Pope et al. prepared an unprecedented gigantic water-soluble supramolecule $[Ce_{16}(H_2O)_{36}(B\text{-}\alpha\text{-}AsW_9O_{33})_{12}(WO_2)_4(W_2O_6)_8(W_5CeO_{18})_4]^{76-}$ incorporating 12 $(B\text{-}\alpha\text{-}AsW_9O_{33})$ and 4 $\{W_5O_{18}\}$ fragments by the one-pot self-assembly of $Na_2WO_4{\cdot}2H_2O$, As_2O_3, and $Ce(NO_3)_3{\cdot}6H_2O$.[6] Later, they isolated a family of tetrameric cryptand RECATs $[(H_2O)_{11}RE(RE_2OH)(B\text{-}\alpha\text{-}AsW_9O_{33})_4(WO_2)_4]^{20-}$ (RE = Ce^{III}, Nd^{III}, Sm^{III}, Gd^{III}) by combining RE cations with the cyclic precursor $[(B\text{-}\alpha\text{-}AsW_9O_{33})_4(WO_2)_4]^{28-}$ together.[7] Wang et al. utilized the preformed $\{[\{Ce_2O(H_2O)_5\}\{WO(H_2O)\}\{AsW_9O_{33}\}_2]_2\}^{16-}$ precursor to react with α-alanine (ala), leading to the isolation of a unique ala-including cryptand $[Ce_4As_4W_{44}O_{151}(ala)_4(OH)_2(H_2O)_{10}]^{12-}$ consisting of four $\{B\text{-}\alpha\text{-}AsW_9O_{33}\}$, two $\{WO_2\}$, two $\{W_2O_5(ala)\}$, a $\{W_2O_5(OH)_2\}$, and two $\{Ce_2(H_2O)_5(ala)\}$ segments.[8] Patzke et al. obtained a class of novel inorganic high nuclear RECAT nanoclusters $[Gd_8As_{12}W_{124}O_{432}(H_2O)_{22}]^{60-}$,[9] $[Cs\subset RE_6As_6W_{63}O_{218}(H_2O)_{14}(OH)_4]^{25-}$ (RE = Eu^{III}, Gd^{III}, Tb^{III}, Dy^{III}, Ho^{III}, Er^{III}),[10] and $[RE_{16}As_{16}W_{164}O_{576}(OH)_8(H_2O)_{42}]^{80-}$ (RE = Eu^{III},

Received: January 9, 2016
Published: April 5, 2016

DOI: 10.1021/acs.inorgchem.6b00061
Inorg. Chem. 2016, 55, 3881−3893

Gd^{III}, Tb^{III}, Dy^{III}, Ho^{III})[11] by the systematic reactions of the dilacunary $[As_2W_{19}O_{67}(H_2O)]^{14-}$ precursor and various RE cations. Boskovic and collaborators synthesized two acetate containing POM-supported polynuclear Ln complexes $[Gd_6As_6W_{65}O_{229}(OH)_4(H_2O)_{12}(OAc)_2]^{38-}$ and $[Yb_{10}As_{10}W_{88}O_{308}(OH)_8(H_2O)_{28}(OAc)_4]^{40-}$ from one-pot reactions of $[B\text{-}\alpha\text{-}AsW_9O_{33}]^{9-}$ and Gd^{3+}/Yb^{3+} cations in the NaOAc/AcOH buffer and preliminarily studied their magnetic properties.[12] Subsequently, by stepwise assembly strategy of the adaptive $[As_2W_{19}O_{67}(H_2O)]^{14-}$ precursor with RE cations in the participation of diverse aromatic or aliphatic organic ligands, Boskovic's group and Niu's group communicated several organic−inorganic hybrid multinuclear RE encapsulated AT aggregates with interesting structural characteristics coupled with intriguing optical properties and magnetic behaviors such as pic-sensitizing luminescent $\{Tb_8(pic)_6(H_2O)_{22}(B\text{-}\beta\text{-}AsW_8O_{30})_4[WO_2(pic)]_6\}^{12-}$,[13] gly ligated $[RE_4As_5W_{40}O_{144}(H_2O)_{10}(gly)_2]^{21-}$ (RE = Gd^{III}, Tb^{III}, Dy^{III}, Ho^{III}, Y^{III}; gly = glycine),[14] pydc-bridging $[As_6W_{58}O_{206}Ce_4(pydc)(H_2O)_6]^{38-}$ (H_2pydc = pyridine-2,3-dicarboxylic acid),[15] tartrate-bridging $[RE_2(C_4H_4O_6)(C_4H_2O_6)(AsW_9O_{33})]_2^{18-}$ (RE = Ho^{III}, Er^{III}, Tm^{III}, Yb^{III}, Lu^{III}, Y^{III}),[16] and citric-functionalized $\{RE_3(H_2O)_7[RE_2(H_2O)_4As_2W_{19}O_{68}(WO_2)_2(C_6O_7H_4)_2]_3\}^{33-}$ (RE = Y^{III}, Tb^{III}, Dy^{III}, Ho^{III}, Er^{III}, Tm^{III}, Yb^{III}, Lu^{III}).[17] In recent years, the search and investigation on AT-based TM−RE heterometallic species has attracted considerable attention. For example, in 2007, Wang's group addressed an inorganic sandwich-type Mn−Ce heterometallic species $\{Mn_5[Ce_4As_4W_{41}O_{149}]_2\}^{46-}$, in which two cryptand $[Ce_4As_4W_{41}O_{149}]^{24-}$ fragments are connected together by a $[Mn(H_2O)_4]^{2+}$ linker.[8] In 2012, we made four types of organic−inorganic hybrid AT-based TM−RE heterometallic derivatives by reaction of the $[A\text{-}\alpha\text{-}AsW_9O_{34}]^{9-}$ precursor with copper and RE cations in the presence of organoamine ligands under hydrothermal conditions and examined their photodegradation activities to rhodamine-B.[18] Very recently, two types of novel tetra-Fe^{III} substituted sandwich-type ATs with supporting RE pendants have also been synthesized by us.[19]

It is very obvious that there are very few reports that trigonal pyramidal $\{AsO_3\}$ groups work as bridges or connectors in the construction of AT-based aggregates and frameworks,[5] although a large number of TM or RE containing ATs and AT-based TM−RE heterometallic species have been already obtained to date. This background is of great interest to us and provides us with an excellent opportunity. We, recently, have concentrated on investigating the reaction system of sodium tungstate, sodium arsenite, and RE salts in the participation of an organic solubilizing agent such as dimethylamine hydrochloride to prepare novel trigonal pyramidal $\{AsO_3\}$ bridging multi-RE incorporated AT aggregates with interesting optical properties by a one-step synthetic procedure based on the following ideas: (a) In order to achieve the goal of trigonal pyramidal $\{AsO_3\}$ groups as connectors during the course of the structural construction, we deliberately increased the dosage of sodium arsenite in the reaction process. (b) The lone electron pair stereochemical effect of the As^{III} atom can hamper in situ generated AT fragments to form the closed Keggin units, which facilitates combination with optically active RE ions into ploy(POM) clusters, giving birth to multi-RE incorporated AT aggregates with optical performances. (c) In the process of our experiments, we found that dimethylamine hydrochloride can to some extent increase the solubility of RE cations in the system of sodium tungstate, sodium arsenite, and water. Herein, we report a family of $\{AsO_2(OH)\}$ bridging RECAT aggregates $[H_2N(CH_3)_2]_8Na_8\{[W_3RE_2(H_2O)_8AsO_8(OH)][B\text{-}\alpha\text{-}AsW_9O_{33}]_2\}_2\cdot 65H_2O$ [RE = Eu^{III} (**1**), Gd^{III} (**2**), Tb^{III} (**3**), Dy^{III} (**4**), Ho^{III} (**5**), Y^{III} (**6**)]. To the best of our knowledge, they stand for the infrequent trigonal pyramidal $\{AsO_2(OH)\}$ connecting poly(AT) aggregates. The thermal stability of **1**, **4**, and **6** has been carefully studied by the combined utilization of variable-temperature IR spectra, variable-temperature powder X-ray diffraction (PXRD) spectra, and the color change of samples obtained at different temperatures. Furthermore, the solid-state luminescence properties and the lifetime decay curves of **1**, **3**, and **4** have been measured at room temperature and discussed in detail.

EXPERIMENTAL SECTION

Materials and Methods. All chemicals were commercially purchased and used without further purification. Carbon, hydrogen, and nitrogen elemental analyses were performed on a Vario EL Cube CHNS analyzer. Inductively coupled plasma atomic emission spectrometry (ICP-AES) was carried out on a Perkin−Elmer Optima 2000 ICP-AES spectrometer. IR spectra were collected from solid samples palletized with KBr on a Perkin-Elmer FT-IR spectrometer in the range 400−4000 cm^{-1}. PXRD patterns were recorded on a Bruker D8 ADVANCE apparatus with Cu Kα radiation (λ = 1.54056 Å). Photoluminescence spectra and lifetimes were recorded using an FLS 980 Edinburgh Analytical Instrument apparatus equipped with a 450 W xenon lamp and a μF900H high energy microsecond flashlamp as the excitation sources. TG analyses were performed under a N_2 atmosphere on a Mettler-Toledo TGA/SDTA 851^e instrument with a heating rate of 10 °C min^{-1} from 25 to 800 °C.

*Synthesis of $[H_2N(CH_3)_2]_8Na_8[W_3Eu_2(H_2O)_8AsO_8(OH)][B\text{-}\alpha\text{-}AsW_9O_{33}]_2\}_2\cdot 65H_2O$ (**1**).* $Na_2WO_4\cdot 2H_2O$ (1.201 g, 3.642 mmol) and dimethylamine hydrochloride (0.702 g, 8.58 mmol) were dissolved in 20 mL of distilled water with stirring. $NaAsO_2$ (1 mL, 1 moL L^{-1}) was then added to the solution, and the pH of the resulting solution was adjusted to 3.0 by using HCl (6 mol L^{-1}). Then, $Eu(NO_3)_3\cdot 6H_2O$ (0.204 g, 0.457 mmol) was added into the solution. After the pH was adjusted to 3.0 again, the system was stirred for another 30 min and then filtered. Slow evaporation of the filtrate at ambient temperature resulted in the colorless prism crystals of **1** in about 2 weeks. Yield: 0.253 g (22.11%) based on $Na_2WO_4\cdot 2H_2O$. Anal. Calcd (%) for **1**: C, 1.46; H, 1.74; N, 0.85; Na, 1.39; W, 58.52; Eu, 4.61; As, 3.41. Found: C, 1.57 H, 1.86; N, 0.94; Na, 1.43; W, 57.94; Eu, 4.70; As, 3.52.

*Synthesis of $[[H_2N(CH_3)_2]_8Na_8\{[W_3Gd_2(H_2O)_8AsO_8(OH)][B\text{-}\alpha\text{-}AsW_9O_{33}]_2\}_2\cdot 65H_2O$ (**2**).* The synthesis process of **2** is similar to that of **1**, except that $Eu(NO_3)_3\cdot 6H_2O$ (0.204 g, 0.457 mmol) was replaced by $Gd(NO_3)_3\cdot 6H_2O$ (0.201 g, 0.445 mmol). The colorless prism crystals of **2** were obtained. Yield: 0.234 g (20.43%) based on $Na_2WO_4\cdot 2H_2O$. Anal. Calcd (%) for **2**: C, 1.45; H, 1.74; N, 0.85; Na, 1.39; W, 58.43; Gd, 4.76; As, 3.40 (%). Found: C, 1.62 H, 1.79; N, 0.92; Na, 1.47; W, 58.04; Gd, 4.69; As, 3.32 (%).

*Synthesis of $[H_2N(CH_3)_2]_8Na_8\{[W_3Tb_2(H_2O)_8AsO_8(OH)][B\text{-}\alpha\text{-}AsW_9O_{33}]_2\}_2\cdot 65H_2O$ (**3**).* The synthesis process of **3** is similar to that of **1**, except that $Eu(NO_3)_3\cdot 6H_2O$ (0.204 g, 0.457 mmol) was replaced by $Tb(NO_3)_3\cdot 6H_2O$ (0.202 g, 0.446 mmol). The colorless prism crystals of **3** were obtained. Yield: 0.306 g (26.69%) based on $Na_2WO_4\cdot 2H_2O$. Anal. Calcd (%) for **3**: C, 1.45; H, 1.74; N, 0.85; Na, 1.39; W, 58.40; Tb, 4.81; As, 3.40 (%). Found: C, 1.58 H, 1.82; N, 0.93; Na, 1.52; W, 57.97; Tb, 4.52; As, 3.27 (%).

*Synthesis of $[H_2N(CH_3)_2]_8Na_8\{[W_3Dy_2(H_2O)_8AsO_8(OH)][B\text{-}\alpha\text{-}AsW_9O_{33}]_2\}_2\cdot 65H_2O$ (**4**).* The synthesis process of **4** is similar to that of **1**, except that $Eu(NO_3)_3\cdot 6H_2O$ (0.204 g, 0.457 mmol) was replaced by $Dy(NO_3)_3\cdot 6H_2O$ (0.197 g, 0.432 mmol). The colorless prism crystals of **4** were obtained. Yield: 0.287 g (25.01%) based on $Na_2WO_4\cdot 2H_2O$. Anal. Calcd (%) for **4**: C, 1.45; H, 1.74; N, 0.85; Na, 1.39; W, 58.34; Dy, 4.91; As, 3.40 (%). Found: C, 1.54 H, 1.84; N, 0.95; Na, 1.54; W, 57.87; Dy, 4.61; As, 3.19 (%).

DOI: 10.1021/acs.inorgchem.6b00061
Inorg. Chem. 2016, 55, 3881−3893

Table 1. Crystallographic Data and Structure Refinements for 1−6

	1	2	3	4	5	6
empirical formula	$C_{16}H_{228}As_6Eu_4N_8Na_8O_{231}W_{42}$	$C_{16}H_{228}As_6Gd_4N_8Na_8O_{231}W_{42}$	$C_{16}H_{228}As_6Tb_4N_8Na_8O_{231}W_{42}$	$C_{16}H_{228}As_6Dy_4N_8Na_8O_{231}W_{42}$	$C_{16}H_{228}As_6Ho_4N_8Na_8O_{231}W_{42}$	$C_{16}H_{228}As_6Y_4N_8Na_8O_{231}W_{42}$
fw	13193.04	13214.20	13220.88	13235.20	13244.92	12940.84
cryst syst	triclinic	triclinic	triclinic	triclinic	triclinic	triclinic
space group	$P\bar{1}$	$P\bar{1}$	$P\bar{1}$	$P\bar{1}$	$P\bar{1}$	$P\bar{1}$
a, Å	14.3527(10)	14.3783(10)	14.3786(7)	14.3671(6)	14.3563(10)	14.3606(10)
b, Å	19.2366(13)	19.2921(13)	19.2779(9)	19.2919(8)	19.2851(13)	19.2822(14)
c, Å	22.4034(15)	22.4977(17)	22.5171(11)	22.5248(9)	22.5210(16)	22.5192(17)
α, deg	78.0000(10)	78.6700(10)	78.8840(10)	78.8700(10)	78.8610(10)	78.8970(10)
β, deg	86.2420(10)	86.2430(10)	86.4870(10)	86.4870(10)	86.5150(10)	86.5170(10)
γ, deg	83.7930(10)	83.6820(10)	83.8090(10)	83.8100(10)	83.7990(10)	83.7970(10)
V, Å^{-3}	6009.0(7)	6075.6(7)	6083.4(5)	6084.8(4)	6076.9(7)	6078.0(8)
Z	1	1	1	1	1	1
μ, mm^{-1}	21.984	21.802	21.847	21.908	22.009	21.662
F(000)	5874	5878	5882	5886	5890	5778
T, K	296(2)	296(2)	296(2)	296(2)	296(2)	296(2)
limiting indices	$-17 \le h \le 17$	$-17 \le h \le 17$	$-17 \le h \le 17$	$-17 \le h \le 17$	$-17 \le h \le 16$	$-17 \le h \le 17$
	$-20 \le k \le 22$	$-15 \le k \le 22$	$-22 \le k \le 22$	$-22 \le k \le 21$	$-22 \le k \le 15$	$-22 \le k \le 18$
	$-18 \le l \le 26$	$-26 \le l \le 26$	$-26 \le l \le 22$	$-26 \le l \le 22$	$-26 \le l \le 25$	$-26 \le l \le 26$
no. of reflns collected	30783	31218	31336	31203	31134	31160
no. of indep reflns	20910	21187	21225	21153	21198	21254
R_{int}	0.0486	0.0596	0.0390	0.0417	0.0425	0.0596
data/restrains/params	20910/77/1154	21187/134/1160	21225/29/1160	21153/23/1160	21198/35/1161	21254/129/1137
GOF on F^2	1.033	1.036	1.043	1.025	1.085	1.007
final R indices [$I > 2\sigma(I)$]	R1 = 0.0502	R1 = 0.0598	R1 = 0.0453	R1 = 0.0490	R1 = 0.0498	R1 = 0.0591
	wR2 = 0.1252	wR2 = 0.1430	wR2 = 0.1213	wR2 = 0.1254	wR2 = 0.1155	wR2 = 0.1504
R indices (all data)	R1 = 0.0702	R1 = 0.0875	R1 = 0.0612	R1 = 0.0655	R1 = 0.0785	R1 = 0.0824
	wR2 = 0.1332	wR2 = 0.1539	wR2 = 0.1284	wR2 = 0.1331	wR2 = 0.1249	wR2 = 0.1621

Synthesis of $[H_2N(CH_3)_2]_8Na_8\{[W_3Ho_2(H_2O)_8AsO_8(OH)][B\text{-}\alpha\text{-}AsW_9O_{33}]_2\}_2\cdot 65H_2O$ (5). The synthesis process of **5** is similar to that of **1**, except that $Eu(NO_3)_3\cdot 6H_2O$ (0.204 g, 0.457 mmol) was replaced by $Ho(NO_3)_3\cdot 6H_2O$ (0.200 g, 0.436 mmol). The light yellow prism crystals of **5** were obtained. Yield: 0.342 g (29.78%) based on $Na_2WO_4\cdot 2H_2O$. Anal. Calcd (%) for **5**: C, 1.45; H, 1.74; N, 0.85; Na, 1.39; W, 58.30; Ho, 4.88; As, 3.39 (%). Found: C, 1.62 H, 1.79; N, 0.96; Na, 1.47; W, 58.17; Ho, 4.61; As, 3.09 (%).

Synthesis of $[H_2N(CH_3)_2]_8Na_8\{[W_3Y_2(H_2O)_8AsO_8(OH)][B\text{-}\alpha\text{-}AsW_9O_{33}]_2\}_2\cdot 65H_2O$ (6). The synthesis process of **6** is similar to **1**, except that $Eu(NO_3)_3\cdot 6H_2O$ (0.204 g, 0.457 mmol) was replaced by $Y(NO_3)_3\cdot 6H_2O$ (0.194 g, 0.507 mmol). The colorless prism crystals of **6** were obtained. Yield: 0.361 g (32.17%) based on $Na_2WO_4\cdot 2H_2O$. Anal. Calcd (%) for **6**: C, 1.49; H, 1.78; N, 0.87; Na, 1.42; W, 59.67; Y, 2.75; As, 3.47 (%). Found: C, 1.61 H, 1.85; N, 0.98; Na, 1.56; W, 58.97; Y 2.61; As, 3.32 (%).

X-ray Crystallography. A good single crystal of **1**, **2**, **3**, **4**, **5**, or **6** was prudentially picked under an optical microscope and sealed to a glass tube closed at both ends. Single-crystal X-ray diffraction intensity data for **1**−**6** were collected on a Bruker APEX-II CCD detector at 296(2) K with Mo Kα monochromated radiation (λ = 0.71073 Å). Direct methods were used to solve their structures and locate the heavy atoms using the SHELXTL-97 program package.[20] The remaining atoms were found from successive full-matrix least-squares refinements on F^2 and Fourier syntheses. Lorentz polarization and SADABS corrections were applied. All hydrogen atoms attached to carbon and nitrogen atoms were geometrically placed and refined isotropically as a riding model using the default SHELXTL parameters. No hydrogen atoms associated with water molecules were located from the difference Fourier map. All non-hydrogen atoms were refined anisotropically except for some sodium, oxygen, nitrogen, and carbon atoms and water molecules. During the course of structural refinements, 44 lattice water molecules for **1**−**6** per molecule were found from the Fourier maps. However, there are still solvent accessible voids in the check cif reports of crystal structures, indicating that some lattice water molecules should exist in the structures that cannot be found from the weak residual electron peaks. These water molecules are highly disordered, and attempts to locate and refine them were unsuccessful. On the basis of elemental analyses and TG analyses, 21 lattice water molecules were directly added to each molecular formula. The crystallographic data and structural refinements for **1**−**6** are listed in Table 1, and CCDC reference nos. 1439023−1439028 are for **1**−**6**. These data can be obtained free of charge from the Cambridge Crystallographic Data Centre via www.ccdc.cam.ac.uk/data_request/cif.

RESULTS AND DISCUSSION

Synthesis and Structure. In the past several decades, there are numerous reported TM or RE containing ATs and AT-based TM−RE heterometallic species; however, few studies have been devoted to the trigonal pyramidal $\{AsO_3\}$ bridging ATs, let alone $\{AsO_3\}$-bridging multi-RE-containing ATs. As a result, the elaborate design and preparation of novel $\{AsO_3\}$-bridging multinuclear RECATs remains a great challenge. The main difficulty in manufacturing $\{AsO_3\}$-bridging multinuclear RECATs is that RE-substituted POMs often have high surface negative charges, which leads to the introduction of negatively charged $\{AsO_3\}$ groups becoming more difficult. In order to resolve this difficulty, according to the chemical equilibrium principle, the dosage of sodium arsenite has been increased in the reaction process, which contributes to much more negatively charged $\{AsO_3\}$ groups in the resulting multinuclear RECATs that provide a good possibility for the formation of

DOI: 10.1021/acs.inorgchem.6b00061
Inorg. Chem. 2016, 55, 3881−3893

{AsO_3} bridges; simultaneously, many more RE cations can also be incorporated into the resulting outcomes on account of the requirement of charge balance. Actually, the existence of two additional facts (the combination of oxyphilic RE ions with oxygen-rich lacunary AT fragments easily leads to amorphous precipitates instead of crystallization, and the solubility of RE ions in the lacunary AT reaction system is very low, which makes the synthesis of multinuclear RECATs become uneasy) also can to some extent increase the difficulty in manufacturing {AsO_3}-bridging multinuclear RECATs; to overcome these two obstacles, we first utilized the assembly reaction strategy of the simple starting materials such as $Na_2WO_4{\cdot}2H_2O$, Na_2AsO_2, and $RE(NO_3)_3{\cdot}6H_2O$ in the acidic (pH = 3.0) conditions to realize the combination of in situ generated lacunary AT fragments and RE ions, and then controlled the lower concentration of the reaction solution, which prolonged the crystallization time, thus effectively avoided formation of the amorphous precipitates. Furthermore, dimethylamine hydrochloride was used as the solubilizing agent to enhance the solubility of RE cations in the reaction system for meeting the positive charge requirement originating from the import of {AsO_3} bridges. Compounds **1**−**6** were all made by the one-pot reaction of $Na_2WO_4{\cdot}2H_2O$, $NaAsO_2$, dimethylamine hydrochloride, and $RE(NO_3)_3{\cdot}6H_2O$ in a molar ratio of 8.3:2.3:19.6:1.0 in acidic aqueous medium (Scheme 1). The results of parallel experiments reveal that the

Scheme 1. Schematic Synthetic Processes of 1−6

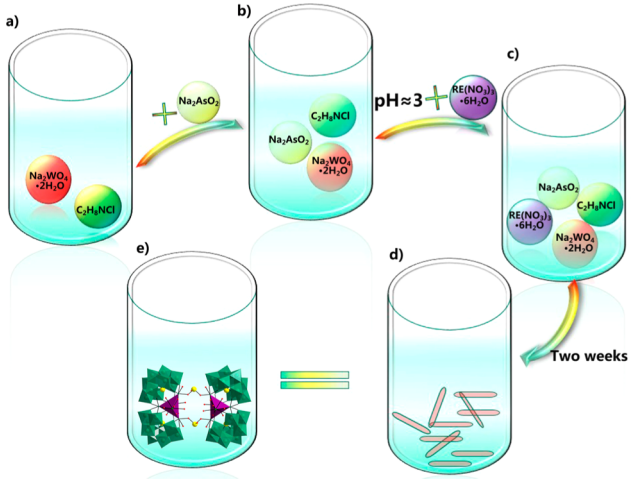

pH value in the range 2.7−3.8 is all beneficial for the formation of **1**−**6**. When the value is adjusted to 3.0 with keeping the other conditions unchanged, their yields are the highest. In addition, we have also explored the effect of the molar ratio of $Na_2WO_4{\cdot}2H_2O$:$NaAsO_2$ on the formation of **1**−**6**. When the molar ratio varies in the range from 2.9 to 4.9, **1**−**6** can be obtained, and their yields are highest when the molar ratio is changed to 3.6. Apart from the above aspects, some efforts were also put into the influence of the usage of RE^{III} cations on the reaction system. When the usage of $RE(NO_3)_3{\cdot}6H_2O$ is changed from 0.154 to 0.271 g, **1**−**6** can be afforded, and their yields are highest when the usage is adjusted to about 0.200 g. Dimethylamine hydrochloride is very indispensable and plays a considerably important role in improving the solubility of RE ions. If dimethylamine hydrochloride is absent, the reaction system will gradually become turbid during the course of stirring, and lots of amorphous precipitation will be formed, leading to failing to get **1**−**6**. On the contrary, when dimethylamine hydrochloride is present, the reaction system can keep clear in the process of stirring, and **1**−**6** will be successfully obtained.

The phase purities of the targeted samples have been characterized by the good agreement of the powder X-ray diffraction patterns with the simulated patterns derived from single-crystal X-ray diffraction. Herein, the comparison of PXRD patterns of **1**−**6** with the simulated X-ray diffraction patterns derived from single-crystal structural analyses as the representative is illustrated in Figure 1. The disparities in

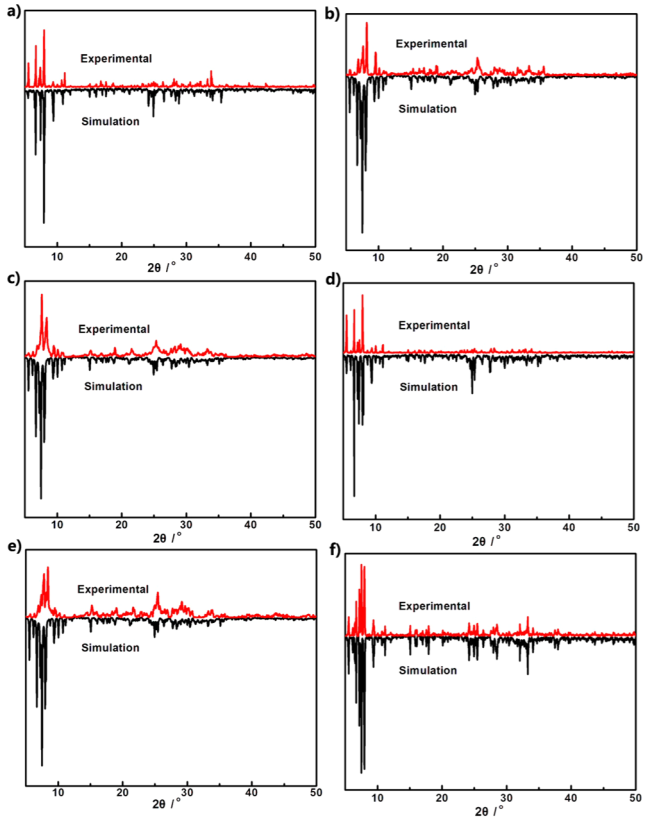

Figure 1. Comparison of PXRD patterns of (a) **1**, (b) **2**, (c) **3**, (d) **4**, (e) **5**, and (f) **6** with the simulated X-ray diffraction patterns derived from single-crystal structural analyses.

intensity between experimental and simulation X-ray diffraction patterns may be because of the variation of the preferred orientation of the powder samples in the process of collecting PXRD patterns.

X-ray single-crystal diffraction reveals that **1**−**6** are isomorphous and crystallize in the triclinic space group $P\bar{1}$. Their polyoxoanionic skeletons contain an unique tetrameric entity of $[(W_3RE_2(H_2O)_8AsO_8(OH))(B\text{-}\alpha\text{-}AsW_9O_{33})_2]_2^{16-}$ constructed from four trivacant Keggin $[\alpha\text{-}AsW_9O_{33}]^{9-}$ fragments and an unseen elliptical $[W_6RE_4(H_2O)_{16}As_2O_{16}(OH)_2]^{20+}$ moiety. In accordance with the effect of lanthanide contraction, the RE−O bond lengths almost decrease as the ionic radius of the RE^{III} cations decreases. Therefore, only the structure of **1** is described as an example below. The molecular structure of **1** consists of an unprecedented trigonal pyramidal {$AsO_2(OH)$} bridging polyoxoanion $[(W_3Eu_2(H_2O)_8AsO_8(OH))(B\text{-}\alpha\text{-}AsW_9O_{33})_2]_2^{16-}$ (**1a**) (Figure 2a and Supporting Information Figure S2), 8 Na^+ cations, 8 monoprotonated $[H_2N(CH_3)_2]^+$

DOI: 10.1021/acs.inorgchem.6b00061
Inorg. Chem. 2016, 55, 3881−3893

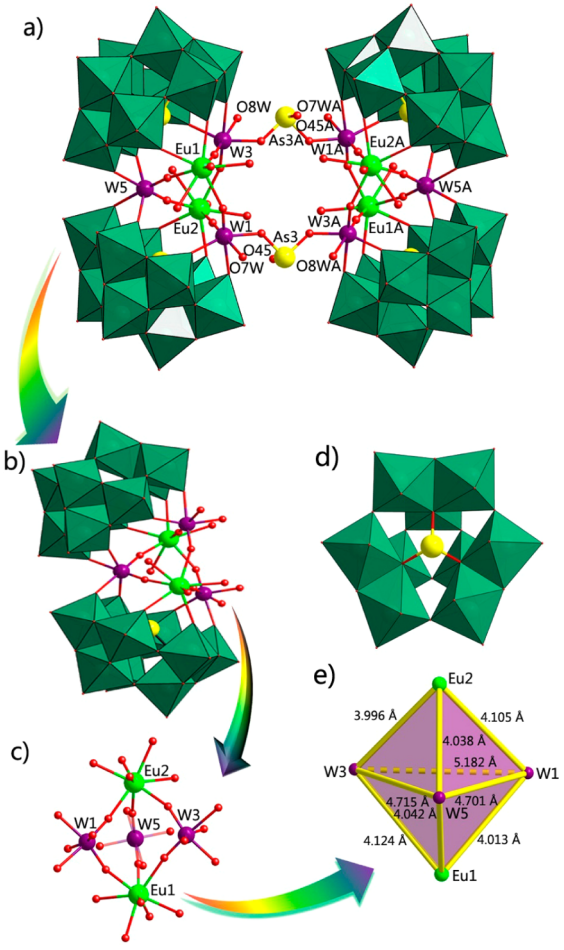

Figure 2. (a) Combined polyhedral and ball-and-stick representation of **1a** with selected numbering scheme. Atoms with A in their labels are symmetrically generated. A: $-x, 2-y, -z$. Lattice water molecules, $[H_2N(CH_3)_2]^+$, and Na^+ are omitted for clarity. (b) The asymmetrical structural unit of **1a**. (c) The pentanuclear $\{W_3Eu_2(H_2O)_8O_7\}$ cluster in **1**. (d) The $[B\text{-}\alpha\text{-}AsW_9O_{33}]^{9-}$ fragment in **1**. (e) The trigonal bipyramid geometry with three W atoms standing on the basal plane and two Eu atoms situated on two vertexes in **1**. Color codes: $\{WO_6\}$ octahedra in trivacant Keggin fragments, sea green; tungsten atoms in the $\{W_3Eu_2(H_2O)_8O_7\}$ cluster, indigo; europium, bright green; arsenic, yellow; oxygen, red.

cations, and 65 lattice water molecules. Bond valence sum (BVS) calculations[21] indicate that the oxidation states of all W, As, and Eu atoms are +6, + 3, and +3, respectively (Table S1). In addition, the BVS value of the terminal O45 atom connected with the As3 atom is 1.06, suggesting that O45 is monoprotonated. As a result, the bridging trigonal pyramidal $\{As3O_2OH\}$ group is written as $\{AsO_2(OH)\}$ in the formula. In addition, terminal O7W and O8W linked to W1 and W3 atoms can also be located by the BVS calculations. On one hand, the infrastructure of **1a** can be described as a fusion of two equivalent dimeric subunits $[(W_3Eu_2(H_2O)_8O_7)(B\text{-}\alpha\text{-}AsW_9O_{33})_2]^{8-}$ (Figure 2b) linked through two μ_2-$\{AsO_2(OH)\}$ connectors. To the best of our knowledge, the linking fashion that connects trigonal pyramidal $\{AsO_2(OH)\}$ groups as μ_2-bridges with two adjacent POM fragments is very rare. The dimeric subunit $[(W_3Eu_2(H_2O)_8O_7)(B\text{-}\alpha\text{-}AsW_9O_{33})_2]^{8-}$ is built by two trivacant Keggin $[\alpha\text{-}AsW_9O_{33}]^{9-}$ fragments sandwiching a pentanuclear $[W_3Eu_2(H_2O)_8O_7]^{10+}$ cluster (Figure 2c) through O–W–O and O–Eu–O–W–O linkers. The $[B\text{-}\alpha\text{-}AsW_9O_{33}]^{9-}$ fragment (Figure 2d) is formed by three edge-sharing W_3O_{13} groups with the help of a central trigonal pyramidal $\{AsO_3\}$ group. The W–O bond lengths vary from 1.685(14) to 2.441(11) Å, and the As–O distances are in the range 1.753(11)–1.802(11) Å. The As^{III} atom has an unshared pair of electrons, and its stereochemical effect can prevent the AT fragments from forming the closed Keggin units and provides a precondition for the derivatization of polymeric AT aggregates. In the dimeric $[(W_3Eu_2(H_2O)_8O_7)(B\text{-}\alpha\text{-}AsW_9O_{33})_2]^{8-}$ subunit, the W5 atom is combined with two $[B\text{-}\alpha\text{-}AsW_9O_{33}]^{9-}$ fragments via four μ_2-O atoms [W–O: 1.910(11)–2.127(11) Å] and two Eu^{3+} ions via two μ_2-O atoms [W–O: 1.715(11)–1.748(11) Å] while each of W1 and W3 atoms links to one $[B\text{-}\alpha\text{-}AsW_9O_{33}]^{9-}$ fragment through two μ_2-O atoms [W–O: 1.925(11)–2.068(10) Å], two Eu^{3+} ions through two μ_2-O atoms [W–O: 1.708(10)–1.774(11) Å], one $\{AsO_2(OH)\}$ group through one μ_2-O atom [W–O: 1.926(12)–1.937(11) Å], and a terminal water ligand [W–O: 2.267(11)–2.318(11) Å]. Evidently, the greatest difference between the octahedral $\{W1O_6\}$, $\{W3O_6\}$, and $\{W5O_6\}$ groups is that each of the W1 and W3 atoms has a terminal water ligand and is in connection with the bridging $\{AsO_2(OH)\}$ group. Although there are two crystallographically independent Eu^{3+} ions in **1a**, both exhibit the eight-coordinate distorted square antiprismatic geometry (Supporting Information Figure S2). The square antiprismatic geometry of the $Eu1^{3+}$ ion is defined by two μ_2-O atoms from one $[B\text{-}\alpha\text{-}AsW_9O_{33}]^{9-}$ fragment [Eu–O: 2.363(12)–2.418(10) Å], three μ_2-O atoms from three $\{WO_6\}$ octahedra in the pentanuclear $[W_3Eu_2(H_2O)_8O_7]^{10+}$ cluster [Eu–O: 2.338(11)–2.428(10) Å], and three terminal coordinated water molecules [Eu–O: 2.389(13)–2.537(13) Å]. Similarly, the square antiprismatic coordination sphere of the $Eu2^{3+}$ ion is also constituted by two μ_2-O atoms from the other $[B\text{-}\alpha\text{-}AsW_9O_{33}]^{9-}$ fragment [Eu–O: 2.364(13)–2.377(11) Å], three μ_2-O atoms from three $\{WO_6\}$ octahedra in the pentanuclear $[W_3Eu_2(H_2O)_8O_7]^{10+}$ cluster [Eu–O: 2.303(11)–2.385(11) Å], and three terminal coordinated water molecules [Eu–O: 2.404(13)–2.536(12) Å]. It should be pointed out that the embedded mode of the pentanuclear $[W_3Eu_2(H_2O)_8O_7]^{10+}$ cluster in the dimeric $[(W_3Eu_2(H_2O)_8O_7)(B\text{-}\alpha\text{-}AsW_9O_{33})_2]^{8-}$ subunit somewhat resembles that of the pentacopper $\{Cu_5(OH)_4(H_2O)_2\}^{6+}$ cluster (Figure 3a) in the dimeric tungstosilicate $[Cu_5(OH)_4(H_2O)_2(A\text{-}\alpha\text{-}SiW_9O_{33})_2]^{10-}$ (7) (Figure 3b) reported by Kortz et al.[22] Evidently, several remarkable structural differences between them are observed: (a) Both trivacant Keggin POM building blocks are different, and the trivacant Keggin POM building block in **1** is $[B\text{-}\alpha\text{-}AsW_9O_{33}]^{9-}$ (Figure 2d) while the trivacant Keggin POM building block in **7** is $[A\text{-}\alpha\text{-}SiW_9O_{34}]^{10-}$ (Figure 3c). (b) The connection modes between two trivacant POM building blocks are distinct, and two trivacant POM building blocks in **1** are bridged by the pentanuclear $[W_3Eu_2(H_2O)_8O_7]^{10+}$ cluster whereas two trivacant POM building blocks in **7** are directly joined together by sharing two μ_3-O atoms as well as the bridging function of the pentacopper $\{Cu_5(OH)_4(H_2O)_2\}^{6+}$ cluster. (c) The chemical components of two pentanuclear metal clusters located in the pockets of the dimeric units are discrepant, and the pentanuclear $[W_3Eu_2(H_2O)_8O_7]^{10+}$ cluster in **1** is heterometallic; nevertheless, the pentanuclear $\{Cu_5(OH)_4(H_2O)_2\}^{6+}$ cluster in **7** is monometallic. (d) The distribution motifs of the five metal atoms in the pentanuclear clusters are distinguishing,

DOI: 10.1021/acs.inorgchem.6b00061
Inorg. Chem. 2016, 55, 3881–3893

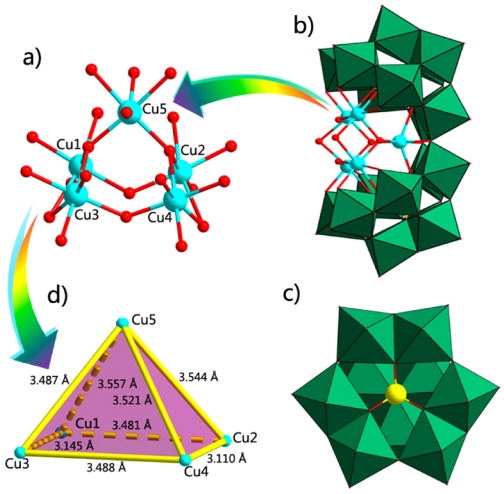

Figure 3. (a) Pentacopper $\{Cu_5(OH)_4(H_2O)_2\}^{6+}$ cluster in **7**. (b) The dimeric tungstosilicate $[Cu_5(OH)_4(H_2O)_2(A\text{-}\alpha\text{-}SiW_9O_{33})_2]^{10-}$ in **7**. (c) The $[A\text{-}\alpha\text{-}SiW_9O_{34}]^{10-}$ fragment in **7**. (d) The tetragonal pyramid geometry with four Cu atoms constituting the basal plane and a Cu atom occupying on the vertex in **7**. Color codes: $\{WO_6\}$ octahedra in trivacant Keggin fragments, sea green; copper, turquoise; arsenic, yellow; oxygen, red.

and the five metal atoms in **1** display the trigonal bipyramid geometry with three W atoms standing on the basal plane and two Eu^{3+} ions situated on two vertexes (Figure 2e); in contrast, the five copper atoms in **7** exhibit the tetragonal pyramid geometry in which four Cu^{2+} ions constitute the basal plane and a Cu^{2+} ion occupies on the vertex (Figure 3d). Additionally, the lacunary $[As_2W_{19}O_{68}]^{16-}$ fragment (Figure 4a) in the $[(W_3Eu_2(H_2O)_8O_7)(B\text{-}\alpha\text{-}AsW_9O_{33})_2]^{8-}$ subunit in **1** is somewhat analogous to the $[As_2W_{19}O_{67}(H_2O)]^{14-}$ precursor (Figure 4b) that was found by Tourné et al. in 1973[23a] and whose structure was determined by Kortz et al. in 2001.[23b] While both formulas are very similar, three conspicuous differences are also seen: (a) Two $[\alpha\text{-}AsW_9O_{33}]^{9-}$ moieties in the $[As_2W_{19}O_{68}]^{16-}$ fragment are asymmetric as a result of the absence of C_2 symmetry; on the contrary, two $[\alpha\text{-}AsW_9O_{33}]^{9-}$ moieties in the $[As_2W_{19}O_{67}(H_2O)]^{14-}$ precursor are symmetric. (b) In comparison with the $[As_2W_{19}O_{67}(H_2O)]^{14-}$ precursor, the bridging $\{WO_6\}$ octahedron connecting two $[\alpha\text{-}AsW_9O_{33}]^{9-}$ moieties in the $[As_2W_{19}O_{68}]^{16-}$ fragment does not have the terminal oxygen atom and the terminal water ligand. (c) The "bite" angle (63.0°) of the $[As_2W_{19}O_{68}]^{16-}$ fragment is far larger than that (29.3°) of the $[As_2W_{19}O_{67}(H_2O)]^{14-}$ precursor mainly because an additional two W and two Eu atoms are encapsulated to the "bite" pocket of the $[As_2W_{19}O_{68}]^{16-}$ fragment in the formation of **1**.

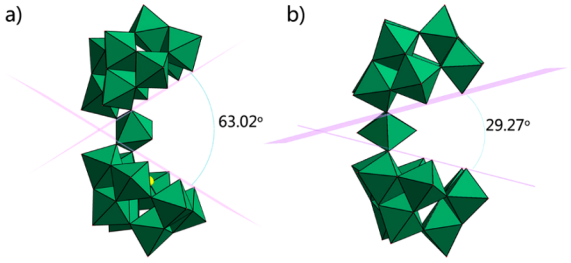

Figure 4. (a) Polyhedral structure of the $[As_2W_{19}O_{68}]^{16-}$ fragment in **1**. (b) The polyhedral structure of the $[As_2W_{19}O_{67}(H_2O)]^{14-}$ precursor.

Alternatively, the polyoxoanionic skeleton of **1a** can be perceived as four $[B\text{-}\alpha\text{-}AsW_9O_{33}]^{9-}$ fragments distributed in the rectangular motif (Supporting Information Figure S3a) anchoring an unprecedented elliptical $[W_6Eu_4(H_2O)_{16}As_2O_{16}(OH)_2]^{20+}$ cluster (Supporting Information Figure S3b) by means of 24 μ_2-O atoms from four $[B\text{-}\alpha\text{-}AsW_9O_{33}]^{9-}$ fragments (Supporting Information Figure S3c). In the $[W_6Eu_4(H_2O)_{16}As_2O_{16}(OH)_2]^{20+}$ cluster, each of two μ_2-$\{AsO_2(OH)\}$ groups directly links two W atoms via two oxygen atoms (Supporting Information Figure S3b). Interestingly, the connection between two trigonal bipyramids defined by three W atoms standing on the basal plane and two Eu atoms situated on two vertexes is through two μ_2-$\{AsO_2(OH)\}$ bridges (Supporting Information Figure S3d), which is uncommon in the coordination chemistry. To put it another way, the polyoxoanion of **1a** is considered as follows: two $[As_2W_{19}O_{68}]^{16-}$ fragments (Figure 5a) in the participation of two $[AsW_2O_{10}(OH)(H_2O)_2]^{6-}$ groups (Figure 5b) form a unique tetrameric AT aggregate $[(W_3AsO_8(OH))(B\text{-}\alpha\text{-}AsW_9O_{33})_2]_2^{28-}$ (Figure 5c), and then four extraneous Eu^{3+} ions are incorporated to the AT aggregate and give rise to the structure of **1a** (Figure 5d).

The 3-D supramolecular packing of **1** along the *a* axis is illustrated in Figure 6a. Monoprotonated $[H_2N(CH_3)_2]^+$ cations are distributed in the space formed by **1a** polyoxoanions and interact with some lattice water molecules and the surface oxygen atoms of AT fragments with N···O distances of 2.77(3)−3.31(2) Å. It can be seen from the simplified 3-D packing arrangement (Figure 6b) that **1a** polyoxoanions are aligned in the − AAA− mode along the *a*, *b*, or *c* axis. The distances between adjacent polyoxoanions are 14.35 Å along the *a* axis, 19.24 Å along the *b* axis, and 22.40 Å along the *c* axis.

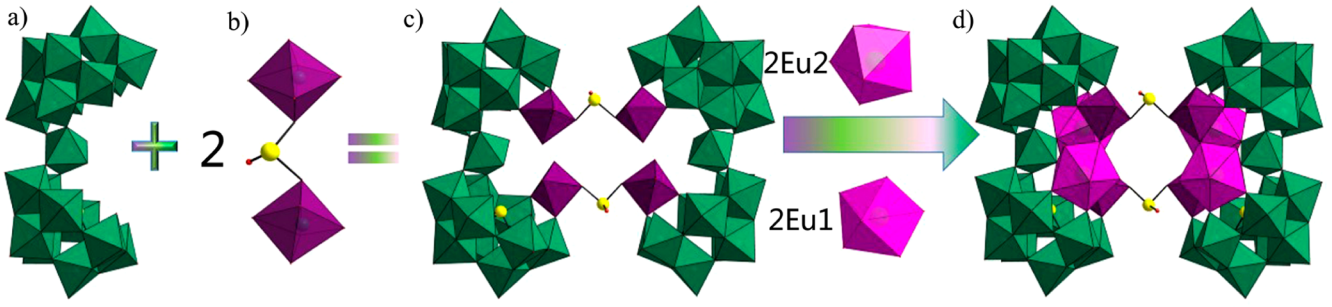

Figure 5. (a) $[As_2W_{19}O_{68}]^{16-}$ fragment in **1**. (b) The $[AsW_2O_{10}(OH)(H_2O)_2]^{6-}$ group in **1**. (c) The skeleton of $[(W_3AsO_8(OH))(B\text{-}\alpha\text{-}AsW_9O_{33})_2]_2^{28-}$. (d) The structure of **1a**.

DOI: 10.1021/acs.inorgchem.6b00061
Inorg. Chem. 2016, 55, 3881−3893

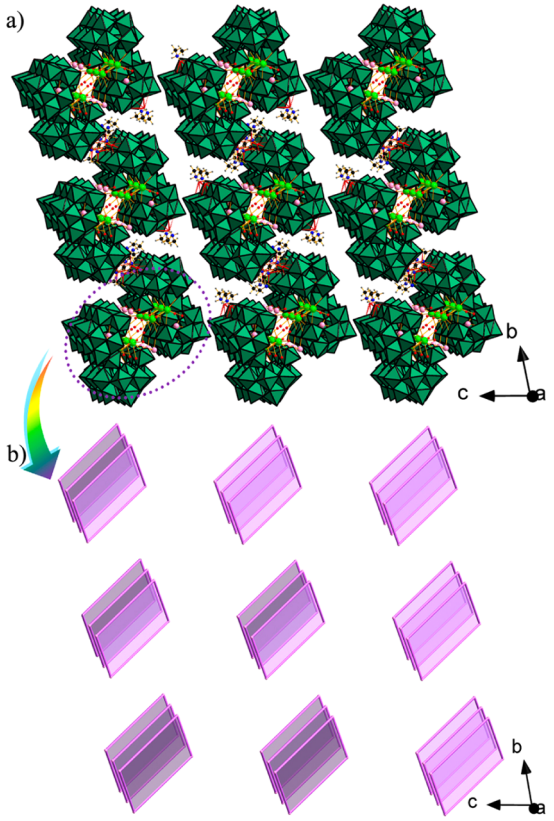

Figure 6. (a) Three-dimensional supramolecular packing of **1** viewed along the *a* axis. Na^+ ions and lattice water molecules are omitted for clarity. (b) The simplified 3-D packing of **1** viewed along the *a* axis.

IR Spectra. IR spectra of **1**−**6** have been recorded between 4000 and 400 cm^{-1} on a Nicolet 170 SXFT-IR spectrometer by utilizing KBr pellets (Supporting Information Figure S4). It is common sense for us that the broad vibration band located in the range 3410−3391 cm^{-1} for **1**−**6** is indicative of the presence of lattice or coordination water molecules.[24a,b] The two weak bands appearing at 3141−3344 and 2772−2797 cm^{-1} are, respectively, assigned to the N−H and C−H stretching vibrations,[24c] illustrating the presence of dimethylamine components. In addition, the existence of the AT fragments of **1**−**6** is also supported by their IR spectral features. Their characteristic vibration bands can be carefully assigned by comparison with the previous literature documenting those characteristic vibration patterns derived from the Keggin AT framework in the low wavenumber region.[25] Specifically, IR spectra of **1**−**6** show four characteristic vibration bands attributable to $\nu(W{-}O_t)$, $\nu(As{-}O_a)$, $\nu(W{-}O_b)$, and $\nu(W{-}O_c)$ which are observed at 947, 863, 787, and 711 cm^{-1} for **1**; 953, 865, 789, and 711 cm^{-1} for **2**; 950, 870, 787, and 711 cm^{-1} for **3**; 953, 868, 787, and 711 cm^{-1} for **4**; 961, 870, 781, and 712 cm^{-1} for **5**; and 953, 868, 783, and 711 cm^{-1} for **6**, respectively. In addition, the RE−O stretching vibrations are absent in the IR region of **1**−**6**, and the possible reason can be on account of predominant ionic interactions between AT fragments and RE cations.[26]

Thermogravimetric (TG) Analysis. In order to examine their thermal stability, the TG behaviors of **1**−**6** were investigated on the crystalline samples under flowing N_2 atmosphere from 25 to 800 °C. As demonstrated in Figure S5 in the Supporting Information, **1**−**6** display the similar continuous three-step weight loss process. From 25 to 150 °C, the first weight loss of 8.93% (calcd 8.87%) for **1**, 8.80% (calcd 8.85%) for **2**, 8.89% (calcd 8.85%) for **3**, 8.61% (calcd 8.84%) for **4**, 8.98% (calcd 8.83%) for **5**, and 9.41% (calcd 9.04%) for **6** approximately corresponds to the release of 65 lattice water molecules. The second weight loss observed between 150 and 600 °C is 5.06% (calcd 5.59%) for **1**, 5.14% (calcd 5.59%) for **2**, 5.72% (calcd 5.58%) for **3**, 5.45% (calcd 5.58%) for **4**, 5.68% (calcd 5.57%) for **5**, and 5.72% (calcd 5.70%) for **6**, respectively, which is attributed to the loss of 16 coordination water molecules, the dehydration of 10 protons, and the removal of 8 dimethylamine groups. The third weight loss in the range 600−800 °C is 4.69% (calcd 4.49%) for **1**, 4.13% (calcd 4.49%) for **2**, 4.41% (calcd 4.49%) for **3**, 4.14% (calcd 4.48%) for **4**, 4.27% (calcd 4.48%) for **5**, and 4.48% (calcd 4.58%) for **6**, respectively, which is assigned to the sublimation of three As_2O_3. Overall, the total weight loss is 18.68% (calcd 18.96%) for **1**, 18.06% (calcd 18.93%) for **2**, 19.02% (calcd 18.92%) for **3**, 18.20% (calcd 18.90%) for **4**, 18.93% (calcd 18.88%) for **5**, and 19.61% (calcd 19.33%) for **6**. Apparently, the experimental values coincide with the theoretical values.

In order to deeply understand their thermal decomposition process, **1**, **4**, and **6** as representatives have been studied by means of IR spectra, PXRD patterns, and visual inspection of color change of the samples. According to their TG curves, we analyzed the samples at 25, 50, 100, 250, 430, 600, and 750 °C. As shown in Figure S6 in the Supporting Information, when the temperature was heated to 250 °C, the color of three samples began to change from colorless to brilliant yellow, which may result from the release of lattice and coordination water molecules. Upon temperature increasing to 430 °C, three compounds have become black possibly because of the carbonization of dimethylamine components under N_2 atmosphere. At 750 °C, three samples became yellowish-green, indicating that all the dimethylamine components have been removed, leaving the formation of new mixed phases due to the decomposition of the polyoxoanionic skeletons of **1**, **4**, and **6**.

It can be seen from Figure 7 that there is no obvious change in the PXRD patterns of three samples when temperature gradually increases from 25 to 100 °C, demonstrating that the crystalline structures of **1**, **4**, and **6** remain almost unchanged in spite of the liberation of some lattice water molecules, which are also consolidated by the excellent conformity of the IR spectra collected at 100 °C with those collected at 25 °C (Figure 8). Upon heating to 250 °C, the removal of all the lattice water molecules and some coordination water molecules leads to the efflorescence of the crystalline samples of **1**, **4**, and **6**, which makes their PXRD patterns at 250 °C worse; however, their polyoxoanionic skeletons are still maintained, which can be certified by the presence of some characteristic peaks derived from polyoxoanionic skeletons in the range of low diffraction angles in the PXRD spectra and the good agreement of the IR spectra collected at 250 °C with those recorded at 25 °C. When the temperature is elevated to 430 °C, those characteristic peaks derived from polyoxoanionic skeletons in the range of low diffraction angles in the PXRD spectra have disappeared, which indicates that the polyoxoanionic skeletons of **1**, **4**, and **6** begin to decompose. This conjecture is also supported by the black color of three samples at 430 °C derived from the carbonization of dimethylamine components and the disappearance of the characteristic vibration bands of $\nu(W{-}O_b)$ and $\nu(W{-}O_b)$ of the polyoxoanionic skeletons and the

DOI: 10.1021/acs.inorgchem.6b00061
Inorg. Chem. 2016, 55, 3881−3893

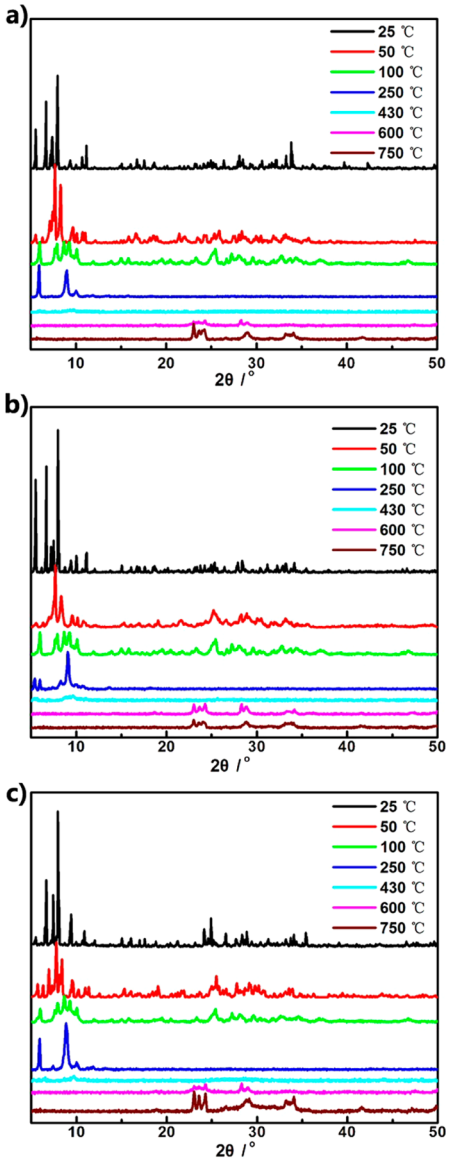

Figure 7. (a) Evolution of the PXRD patterns of samples of **1** at the different temperatures. (b) The evolution of the PXRD patterns of samples of **4** at the different temperatures. (c) The evolution of the PXRD patterns of samples of **4** at the different temperatures.

invisibility of the N−H and C−H stretching vibration bands of dimethylamine components. At 600 °C, the observation of PXRD and IR spectra of three samples suggests that the polyoxoanionic skeletons of **1**, **4**, and **6** have been destroyed. The formation of new mixed phases at 750 °C can also be proved by the yellowish-green color of three samples, the occurrence of a broad band center at 800 cm^{-1} in the 750 °C IR spectra, and the appearance of new diffraction peaks between 20° and 45° in the 750 °C PXRD spectra. Moreover, the residuals at 750 °C of **1**, **4**, and **6** should contain rare-earth oxide components, which have been confirmed by the comparisons of the PXRD spectra of the residuals at 750 °C of **1**, **4**, and **6** with the PXRD spectra of corresponding rare-earth oxides (RE_2O_3) at 750 °C (Supporting Information Figure S7).

Photoluminescence Properties. Since the early discovery in lighting at the end of the 19th century (Auer mantle, flint stones), the invention of the bright red emitting phosphor $Y_2O_3:Eu^{3+}$ at the beginning of the 20th century, and the appearance of the YAG:Nd^{3+} laser in 1964,[27] RE elements have always played a prominent role in lighting and light conversion technologies in areas such as lasers, light-emitting diodes, cathode-ray, plasma displays, optical fibers, optical amplifiers, NIR-emitting materials, and sensory probes.[28] Moreover, the pioneering findings contributed by Dieke, Judd, Wybourne, and others in theoretical and experimental studies of the $4f^n$ electronic structures[29a−d] make many spectroscopic properties of RE^{3+} ions well-understood.[29e−h] To date, some metal oxide luminescent materials such as $BaMgAl_{10}O_{17}:Eu^{2+}$ and $GdMgB_5O_{10}:Ce^{3+},Tb^{3+}$ have been commercially used to the manufacture of blue and green luminescent lamps, respectively.[30] In general, RE-based luminescent materials have aroused extensive interest due to the narrow emission lines ascribed to transitions inside the 4f shell and high color purity originating from RE^{3+} cations. Among the RE^{3+} ions, lanthanide ions (Ln^{3+}) are usually characterized by a gradual filling of the 4f orbitals, from $4f^0$ to $4f^{14}$ (La^{3+} to Lu^{3+}). These electronic $[Xe]4f^n$ configurations (n = 0−14) can lead to various electron energy levels that will produce complicated optical characteristics.[31] On the other hand, their electron energy levels of the 4f orbitals are well-shielded by the outer filled 5s and 5p subshells. As a consequence, except for La^{3+} and Lu^{3+}, each Ln^{3+} ion shows narrow characteristic intra-4f−4f transitions. Therefore, the photoluminescence properties of the solid-state samples of **1**, **3**, and **4** have been investigated at room temperature (Figure

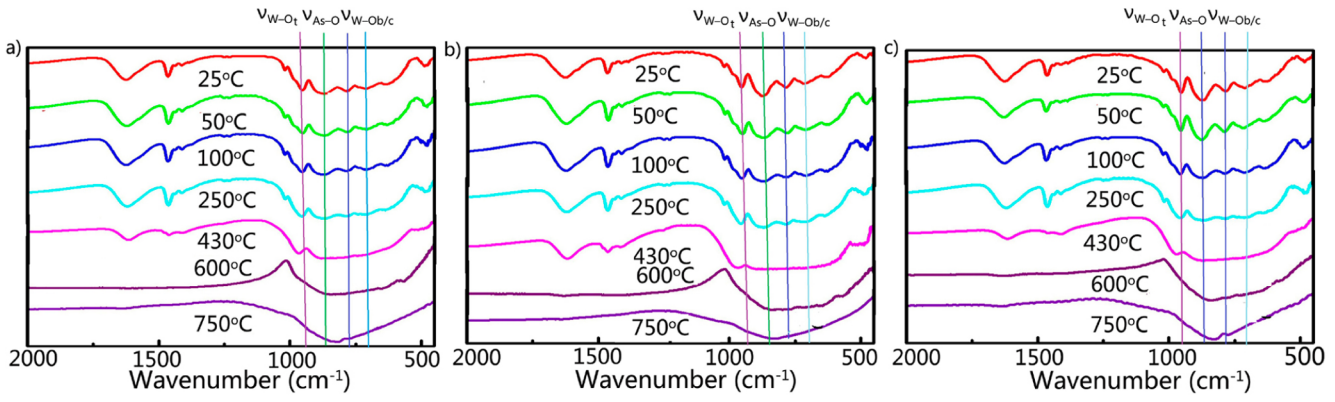

Figure 8. (a) IR spectra of **1** at different temperatures. (b) IR spectra of **4** at different temperatures. (c) IR spectra of **6** at different temperatures. (Color code: $\nu(W-O_t)$, purple vertical line; $\nu(As-O_a)$, green vertical line; $\nu(W-O_{b/c})$, dark blue and light blue vertical lines).

DOI: 10.1021/acs.inorgchem.6b00061
Inorg. Chem. 2016, 55, 3881−3893

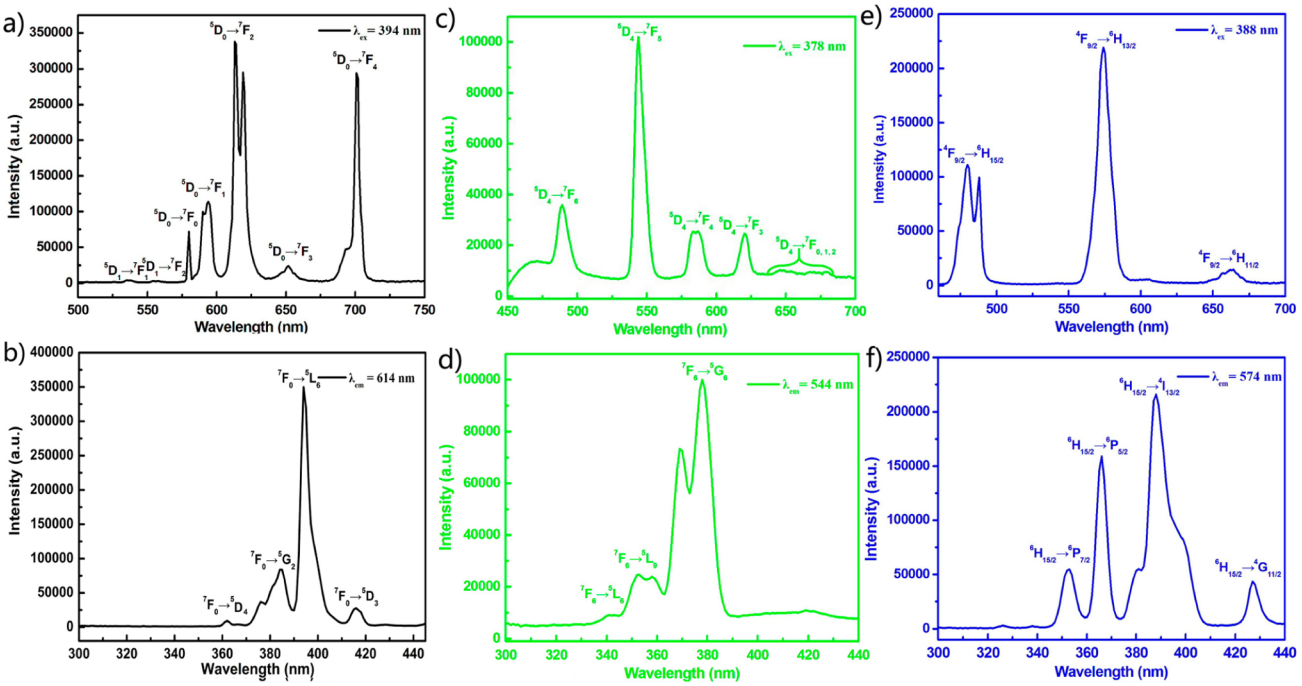

Figure 9. (a) Emission spectrum of **1** under excitation at 394 nm at room temperature. (b) The excitation spectrum of **1** obtained by monitoring the emission at 614 nm. (c) The emission spectrum of **3** under excitation at 378 nm at room temperature. (d) The excitation spectrum of **3** obtained by monitoring the emission at 544 nm. (e) The emission spectrum of **4** under excitation at 388 nm at room temperature. (f) The excitation spectrum of **4** obtained by monitoring the emission at 574 nm.

9). When **1** was excited under an ultraviolet light of 394 nm, the photoluminescence spectrum was observed with seven characteristic emission bands with maxima at 536, 554, 580, 594, 614, 652, and 701 nm (Figure 9a), which are, respectively, attributed to $^5D_1 \rightarrow {}^7F_1$, $^5D_1 \rightarrow {}^7F_2$, $^5D_0 \rightarrow {}^7F_0$, $^5D_0 \rightarrow {}^7F_1$, $^5D_0 \rightarrow {}^7F_2$, $^5D_0 \rightarrow {}^7F_3$, and $^5D_0 \rightarrow {}^7F_4$ transitions of the Eu^{3+} ions. Obviously, the symmetry-forbidden emission $^5D_0 \rightarrow {}^7F_0$ is seen at 580 nm, which indicates that the Eu^{3+} cations in **1** inhabit the low symmetrical coordination environments.[30] It is well-known that $^5D_0 \rightarrow {}^7F_1$ and $^5D_0 \rightarrow {}^7F_2$ are special because of their peculiarity as symmetry-sensitive transitions and are generally known as a magnetic dipole transition and a hypersensitive electric dipole transition, respectively.[32a−c] In general, the magnetic-dipolar $^5D_0 \rightarrow {}^7F_1$ transition is insensitive to the symmetry of crystal field and the local coordination environment while the electric-dipole $^5D_0 \rightarrow {}^7F_2$ transition is very sensitive to the symmetry of crystal field and the local coordination environment. The magnetic-dipole $^5D_0 \rightarrow {}^7F_1$ transition is dominant in a centrosymmetric coordination environment; in contrast, the electronic-dipole $^5D_0 \rightarrow {}^7F_2$ transition is usually the strongest emission band in a ligand field without inversion symmetry.[32d−f] Thus, the intensity ratio of the $I(^5D_0 \rightarrow {}^7F_1)/I(^5D_0 \rightarrow {}^7F_2)$ transitions is greatly sensitive to the local symmetry of the Eu^{3+} cation and generally used as a criterion to check the site symmetry of the Eu^{3+} cation.[33a] In the case of **1**, the intensity ratio of the $^5D_0 \rightarrow {}^7F_2/{}^5D_0 \rightarrow {}^7F_1$ is equal to ca. 3.0, which implies that the Eu^{3+} ions dwell in the low symmetric coordination environments. This conclusion is in good agreement with the case that two crystallographically independent Eu^{3+} ions in **1** exhibit the eight-coordinate distorted square antiprismatic geometry. Furthermore, the dynamic coupling contribution can also contribute to the stronger intensity of $^5D_0 \rightarrow {}^7F_2$ by means of the polarizability of the surrounding atoms or groups of atoms.[33b,c] Additionally, by monitoring the $^5D_0 \rightarrow {}^7F_2$ emission at 614 nm, the excitation spectrum of **1** has been recorded (Figure 9b). The excitation spectrum is dominated by a narrow line at 395 nm, which is attributable to the $^7F_0 \rightarrow {}^5L_6$ transition. Moreover, another three peaks in the range 300−445 nm are observed in the excitation spectrum that involves the intra-4f transitions from the $^7F_0$ ground state to higher energy levels of the Eu^{3+} ions, which are assigned to $^7F_0 \rightarrow {}^5D_4$ (362 nm), $^7F_0 \rightarrow {}^5G_2$ (385 nm), $^7F_0 \rightarrow {}^5D_3$ (416 nm), respectively.[34] The solid-state sample of **3** emits the green luminescence upon excitation at 378 nm. Its emission spectrum displays four obvious and three weak characteristic emission peaks at 489, 544, 587, 621, 647, 668, and 679 nm (Figure 9c), which are, respectively, attributed to the $^5D_4 \rightarrow {}^7F_6$, $^5D_4 \rightarrow {}^7F_5$, $^5D_4 \rightarrow {}^7F_4$, $^5D_4 \rightarrow {}^7F_3$, $^5D_4 \rightarrow {}^7F_2$, $^5D_4 \rightarrow {}^7F_1$, and $^5D_4 \rightarrow {}^7F_0$ transitions of the Tb^{3+} ions.[35] The excitation spectrum of **3** mainly consists of three groups of emission bands with maxima at 340, 352, and 378 nm by monitoring the emission of the Tb^{3+} ions at 544 nm (Figure 9d), which could be referred to the transitions from the $^7F_6$ ground state to the excited states of $^5L_6$, $^5L_9$, and $^5G_6$ levels.[36] Figure 9e shows the emission spectrum of **4** under excitation of an ultraviolet light of 388 nm. The major peaks are located at 481, 574, and 662 nm, which correspond to $^4F_{9/2} \rightarrow {}^6H_{15/2}$, $^4F_{9/2} \rightarrow {}^6H_{13/2}$, and $^4F_{9/2} \rightarrow {}^6H_{11/2}$ transitions, respectively. The $^4F_{9/2} \rightarrow {}^6H_{15/2}$ emission at 481 nm is a magnetic dipole transition, which hardly varies with the crystal field strength or coordination environment around the Dy^{3+} ions. The $^4F_{9/2} \rightarrow {}^6H_{13/2}$ transition at 574 nm is an electric dipole transition and is hypersensitive to the local environments and the crystal field around the Dy^{3+} ions.[37a,b] When the Dy^{3+} ions are located at the low symmetry environments without inversion center, the $^4F_{9/2} \rightarrow {}^6H_{13/2}$ emission is often prominent in the emission spectrum.[37b−e] It can be seen from Figure 9e that the intensity of the $^4F_{9/2} \rightarrow$

DOI: 10.1021/acs.inorgchem.6b00061
Inorg. Chem. 2016, 55, 3881−3893

$^6H_{13/2}$ electric dipole transition is much higher than that of the $^4F_{9/2} \rightarrow {}^6H_{15/2}$ magnetic dipole transition in the emission of spectrum of **4**, illustrating that the Dy^{3+} ions are located at the low symmetrical environments without inversion, which inosculate with the distorted square antiprismatic geometry (D_{4d} point symmetry) of two independent Dy^{3+} ions in **4**. The excitation spectrum of **4** was obtained by monitoring the emission of Dy^{3+} ($^4F_{9/2} \rightarrow {}^6H_{13/2}$) at 574 nm (Figure 9f). It can be observed that the excitation spectrum contains four bands at 353, 367, 388, and 427 nm, which are assigned to typical f−f transitions of the Dy^{3+} ions, that is, the transitions from the $^6H_{15/2}$ ground state to the different excited states $^6P_{7/2}$ (353 nm), $^6P_{5/2}$ (367 nm), $^4I_{13/2}$ (388 nm), and $^4G_{11/2}$ (427 nm), respectively. In addition, in order to obtain the lifetimes, the luminescence decay curves of **1**, **3**, and **4** have been measured (Figure 10 and Supporting Information Figures S8−S10). For **1**, the $^5D_0$ lifetime curve of the Eu^{3+} ions was first monitored under excitation at 394 nm and the most intense emission at 615 nm ($^5D_0 \rightarrow {}^7F_2$) (Figure 10a and Supporting Information Figure S8c). This decay curve can be fitted successfully by a single exponential function as the equation $I = A \exp(-t/\tau)$, where I represents the luminescent intensity, A is the pre-exponential factor, t is the time, and τ is the decay time for the exponential component. The affording lifetime (τ) is 269.00 μs with a pre-exponential factor (A) of 5103.76. The decay time of **1** is very close to that (τ = 0.39 ms) of $Na_{0.5}Cs_{4.5}[Eu(\alpha\text{-}SiW_{11}O_{39})(H_2O)_2]\cdot 23H_2O$,[38] because the coordination spheres of the Eu^{3+} ions in them have close coordination water molecules (three coordination water molecules for the Eu^{3+} ions in **1** and two coordination water molecules for the Eu^{3+} ion in $Na_{0.5}Cs_{4.5}$ $[Eu(\alpha\text{-}SiW_{11}O_{39})(H_2O)_2]\cdot 23H_2O$). The decay time of **1** is much longer than that (τ = 9.51 μs) of $[Eu(H_2O)_8]_2[Fe_4(H_2O)_8(L\text{-}thr)_2(B\text{-}\beta\text{-}AsW_9O_{33})_2]\cdot 20H_2O$,[19] since the number of water ligands on Eu^{3+} ions in **1** is smaller than that in $[Eu(H_2O)_8]_2[Fe_4(H_2O)_8(L\text{-}thr)_2(B\text{-}\beta\text{-}AsW_9O_{33})_2]\cdot 20H_2O$ (the number of water ligands on the Eu^{3+} ions is eight). However, the decay time of **1** is by far shorter than that (τ = 2.440 ms) of $K_{13}[Eu(\alpha\text{-}SiW_{11}O_{39})_2]$,[38] because there is no water ligand on the Eu^{3+} ion in $K_{13}[Eu(\alpha\text{-}SiW_{11}O_{39})_2]$. These observations further manifest that aqua ligands on Eu^{3+} ions consisting of high frequency O−H oscillators tend to quench the luminescence emission.[38b] In order to probe the effect of the different emissions on the lifetimes of the Eu^{3+} ions, the $^5D_0$ lifetime curves of the Eu^{3+} ions were monitored under the excitation at 394 nm and the various emissions at 580, 594, 619, and 701 nm (notably, the peak at 619 nm is a shoulder of the peak at 614 nm and also belongs to the $^5D_0 \rightarrow {}^7F_2$ transition, Figure 10a, and Supporting Information Figures S8a,b,d,e). All the decay curves can be well-fitted with a single-exponential function, giving the corresponding luminescence decay times of 274.83, 271.14, 270.46, and 273.74 μs, respectively (Supporting Information Table S2). Obviously, their decay lifetimes are very similar (Figure 10a), which can illustrate that the decay times of different emissions are greatly related to the same ground state ($^5D_0$) when the effect of nonradiative transitions can be almost negligible. Similarly, the luminescence decay curves of **3** monitored under the excitation at 378 nm and various emissions at 489, 544, 587, and 621 nm can also conform to the fitting of a single exponential function, and their decay times are 149.45, 152.42, 145.76, and 144.11 μs (Figure 10b and Figure S9 and Table S4 in the Supporting Information). The similarity of the decay lifetimes is extremely relevant to the same ground state ($^5D_4$). Different from **1** and **3**, the lifetime curves for monitoring **4** performed under the excitation at 388 nm and emissions at 481 and 574 nm cannot be fitted by a single exponential function but are well-fitted with a second-order exponential function with the following formula: $I = A_1 \exp(t/\tau_1) + A_2 \exp(t/\tau_2)$ (where τ_1 and τ_2 are the fast and slow components of the luminescence lifetimes and A_1 and A_2 are the pre-exponential factors). The fitted luminescence lifetimes τ_1 and τ_2 are 3.19 μs (59.24%) and 11.69 μs (40.76%) for the monitored emission at 481 nm, and 2.93 μs (46.25%) and 9.39

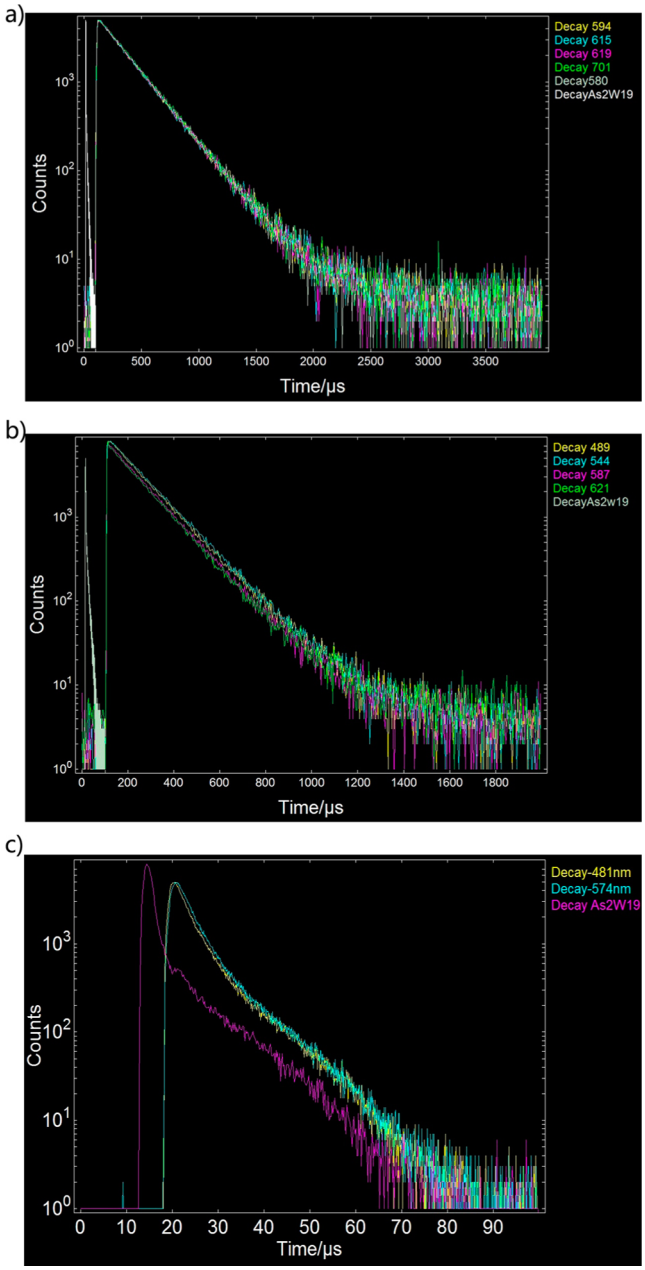

Figure 10. (a) Decay curves of **1** monitored under the excitation at 394 nm and the different emissions at 580, 594, 614, 619, and 701 nm, and the decay curve of As_2W_{19} under the excitation at 394 nm. (b) The decay curves of **3** monitored under the excitation at 378 nm and the different emissions at 489, 544, 587, and 621 nm, and the decay curve of As_2W_{19} under the excitation at 378 nm. (c) The decay curves of **4** monitored under the excitation at 388 nm and the different the emissions at 481 and 574 nm, and the decay curve of As_2W_{19} under the excitation at 388 nm.

DOI: 10.1021/acs.inorgchem.6b00061
Inorg. Chem. 2016, 55, 3881−3893

μs (53.75%) for the monitored emission at 574 nm, respectively (Figure 10c and Supporting Information Figure S10 and Table S6). Therefore, the average decay times (τ^*) can be determined with the following equation: $\tau^* = (A_1\tau_1^2 + A_2\tau_2^2)/(A_1\tau_1 + A_2\tau_2)$.[39] Thus, their average lifetimes are calculated to be 6.66 and 6.40 μs, respectively. In order to further comprehend why the decay times of **1** and **3** belong to the single exponential function while the decay times of **4** obey the second-order exponential function, we measured the emission spectra (Supporting Information Figure S11) and the lifetime decay curves (Figure 10 and Supporting Information Figures S8f, S9e, and S10c) of $K_{14}[As_2W_{19}O_{67}(H_2O)]$ (As_2W_{19}) under the similar conditions to **1**, **3**, and **4** mainly because the structure of the $[As_2W_{19}O_{67}(H_2O)]^{14-}$ segment in As_2W_{19} is very similar to that of the lacunary $[As_2W_{19}O_{68}]^{16-}$ fragments in **1**, **3**, and **4**. Experimental results indicate that the lifetime decay curves of As_2W_{19} under the conditions similar to those of **1**, **3**, and **4** conform to the second-order exponential function, affording τ_1, τ_2, A_1, and A_2 of 0.80 μs (40.85%), 9.39 μs (59.15%), 6031.97, and 745.45 for **1**; 0.87 μs (37.07%), 9.37 μs (62.93%), 4865.52, and 771.02 for **3**; 0.87 μs (37.19%), 9.45 μs (62.81%), 5180.76, and 806.82 for **4**, respectively. The average lifetimes of As_2W_{19} under the similar conditions to **1**, **3**, and **4** are calculated to be 5.88, 6.23, and 6.26 μs, respectively (Supporting Information Tables S3, S5, S7). It can be apparently seen from the above-mentioned results that the lifetimes of **1** and **3** are much longer than those of As_2W_{19}; as a result, the short lifetime contributions derived from AT fragments in **1** and **3** can be negligible, and the lifetimes of **1** and **3** mainly originate from the contribution of RE^{3+} ions and thus abide by the single exponential function. However, the lifetime of AT fragments in **4** is comparable to the overall lifetime of **4**; in this case, the lifetime contribution of AT fragments is not neglected in the overall lifetime investigation of **4**. As a consequence, the overall lifetime of **4** stems from the combined actions of AT fragments and Dy^{3+} ions and adheres to the second-order exponential function.

A good understanding of the trueness of color is rather crucial in the fields of lighting and display devices.[37b] The CIE 1931 diagram is a widely used approach for probing all the possible colors by combining three primary colors, in which the chromaticity coordinates x and y are utilized to identify the precise emission colors of the as-synthesized materials. The CIE chromaticity coordinates for **1**, **3**, and **4** are determined on the basis of their corresponding photoluminescence spectra and are indexed to (0.63828, 0.36022), (0.33947, 0.58007), and (0.37273, 0.41749), respectively (Figure 11). It is observed that **1**, **3**, and **4** display the reddish orange, green, and yellow-green emissions.

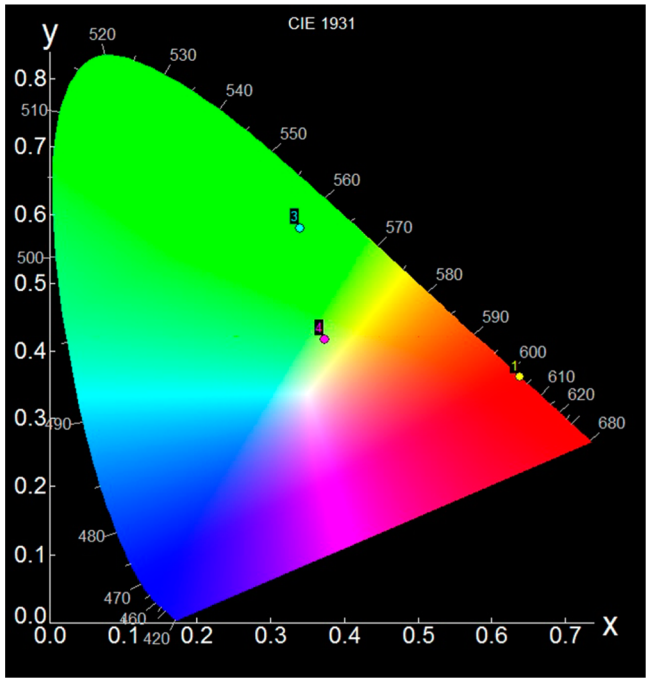

Figure 11. CIE chromaticity diagram of the emissions of **1**, **3**, and **4**.

CONCLUSION

In summary, we have successfully synthesized six arsenic-bridging RE-substituted AT aggregates $[H_2N(CH_3)_2]_8Na_8\{[W_3RE_2(H_2O)_8AsO_8(OH)][B\text{-}\alpha\text{-}AsW_9O_{33}]_2\}_2\cdot 65H_2O$ [RE = Eu^{III} (**1**), Gd^{III} (**2**), Tb^{III} (**3**), Dy^{III} (**4**), Ho^{III} (**5**), Y^{III} (**6**)] by the one-pot reaction of $Na_2WO_4\cdot 2H_2O$, $NaAsO_2$, and $RE(NO_3)_3\cdot 6H_2O$ in the participation of DMAHC in acidic aqueous medium. Interestingly, two μ_2-$\{AsO_2(OH)\}$ groups act as bridges linking two equivalent dimeric subunits $[(W_3RE_2(H_2O)_8O_7)(B\text{-}\alpha\text{-}AsW_9O_{33})_2]^{8-}$, which is rather rare in RE-substituted AT aggregates. The thermal decomposition processes of **1**, **4**, and **6** have been studied by TG curves, variable-temperature IR spectra, and variable-temperature PXRD spectra. The solid-state emission spectrum of **1** exhibits seven characteristic bands that are ascribed to $^5D_1 \rightarrow {}^7F_J$ (J = 1, 2), $^5D_0 \rightarrow {}^7F_J$ (J = 0–4) transitions; the green luminescence of **3** is substantially derived from the $^5D_4 \rightarrow {}^7F_5$ transition, and **4** exhibits three characteristic emission bands that are ascribed to $^4F_{9/2} \rightarrow {}^6H_J$ (J = 15/2, 13/2, 11/2) transitions. The decay curves of **1** and **3** conform to the single exponential function while the decay curve of **4** is fitted by a double-exponential function. The comparative investigations on lifetimes of **1**, **3**, **4**, and As_2W_{19} show that the lifetimes of **1** and **3** dominantly are derived from the contribution of RE ions while the lifetime of **4** is contributed by the cooperative actions of AT fragments and Dy^{3+} ions. This work not only enriches the structural diversity of RE containing AT aggregates, but also provides a useful synthetic strategy that trigonal pyramidal $\{XO_3\}$ groups (X = As^{III}, Sb^{III}, Bi^{III}, Se^{IV}, Te^{IV}) can be utilized as connectors to combine with different POM fragments. Therefore, the starting materials including Sb^{III}, Bi^{III}, Se^{IV}, Te^{IV} atoms will be introduced to the system to construct much more $\{XO_3\}$-bridging RE containing POM aggregates. Moreover, in this system, multifunctional organic ligands will be used as good chromophores to sensitize the luminescence emissions of RE ions.

ASSOCIATED CONTENT

Supporting Information

The Supporting Information is available free of charge on the ACS Publications website at DOI: 10.1021/acs.inorgchem.6b00061.

BVS calculations of W, Ln, and O atoms in **1**; related structural figures; IR spectra, related PXRD patterns, and TG curves of **1**–**6**; the luminescence decay curves of **1**, **3**, and **4**; the emission spectra of As_2W_{19} (PDF)

Crystal data (CIF)

DOI: 10.1021/acs.inorgchem.6b00061
Inorg. Chem. 2016, 55, 3881–3893

AUTHOR INFORMATION

Corresponding Authors

*E-mail: ljchen@henu.edu.cn.
*E-mail: zhaojunwei@henu.edu.cn. Fax: +86-371- 23881589.
*E-mail: ygy@bit.edu.cn. Fax: +86-10-68918572.

Notes

The authors declare no competing financial interest.

ACKNOWLEDGMENTS

This work was supported by the Natural Science Foundation of China (21301049, U1304208, 21571048, 91122028, 21221001, 50872133), the Natural Science Foundation of China for Distinguished Young Scholars (20725101), the 973 Program (2014CB932101 and 2011CB932504), the Natural Science Foundation of Henan Province (142300410451), Program for Science & Technology Innovation Talents in Universities of Henan Province (16HASTIT001), the Postdoctoral Foundation of Henan Province (2014025), the Foundation of State Key Laboratory of Structural Chemistry (20160016), 2014 Special Foundation for Scientific Research Project of Henan University (XXJC20140001), 2012 Young Backbone Teachers Foundation from Henan Province (2012GGJS-027).

REFERENCES

(1) (a) Marrot, J.; Pilette, M. A.; Haouas, M.; Floquet, S.; Taulelle, F.; Lopez, X.; Poblet, J. M.; Cadot, É. *J. Am. Chem. Soc.* **2012**, *134*, 1724. (b) Zhao, Y.; Deng, D.-S.; Ma, L.-F.; Ji, B.-M.; Wang, L.-Y. *Chem. Commun.* **2013**, *49*, 10299. (c) Zheng, S.-T.; Zhang, J.; Li, X.-X.; Fang, W.-H.; Yang, G.-Y. *J. Am. Chem. Soc.* **2010**, *132*, 15102. (d) Heine, J.; Müller-Buschbaum, K. *Chem. Soc. Rev.* **2013**, *42*, 9232. (e) Descalzo, A. B.; Martínez-Mañez, R.; Sancenon, F.; Hoffmann, K.; Rurack, K. *Angew. Chem., Int. Ed.* **2006**, *45*, 5924.

(2) (a) Kortz, U.; Al-Kassem, N. K.; Savelieff, M. G.; Al Kadi, N. A.; Sadakane, M. *Inorg. Chem.* **2001**, *40*, 4742. (b) Kortz, U.; Nellutla, S.; Stowe, A. C.; Dalal, N. S.; van Tol, J.; Bassil, B. S. *Inorg. Chem.* **2004**, *43*, 144. (c) Mbomekalle, I. M.; Keita, B.; Nierlich, M.; Kortz, U.; Berthet, P.; Nadjo, L. *Inorg. Chem.* **2003**, *42*, 5143. (d) Yamase, T.; Fukaya, K.; Nojiri, H.; Ohshima, Y. *Inorg. Chem.* **2006**, *45*, 7698. (e) McGlone, T.; Vilà-Nadal, L.; Miras, H. N.; Long, D.-L.; Poblet, J. M.; Cronin, L. *Dalton Trans.* **2010**, *39*, 11599.

(3) Zhao, J. W.; Shi, D. Y.; Chen, L. J.; Ma, P. T.; Wang, J. P.; Niu, J. Y. *CrystEngComm* **2011**, *13*, 3462.

(4) Zhao, J. W.; Shi, D. Y.; Chen, L. J.; Cai, X. M.; Wang, Z. Q.; Ma, P. T.; Wang, J. P.; Niu, J. Y. *CrystEngComm* **2012**, *14*, 2797.

(5) Zhou, Z.; Zhang, D. D.; Yang, L.; Ma, P. T.; Si, Y. N.; Kortz, U.; Niu, J. Y.; Wang, J. P. *Chem. Commun.* **2013**, *49*, 5189.

(6) Wassermann, K. M.; Dickman, H.; Pope, M. T. *Angew. Chem., Int. Ed. Engl.* **1997**, *36*, 1445.

(7) Wassermann, K.; Pope, M. T. *Inorg. Chem.* **2001**, *40*, 2763.

(8) Chen, W. L.; Li, Y. G.; Wang, Y. H.; Wang, E. B.; Su, Z. M. *Dalton Trans.* **2007**, 4293.

(9) Hussain, F.; Conrad, F.; Patzke, G. R. *Angew. Chem., Int. Ed.* **2009**, *48*, 9088.

(10) Hussain, F.; Spingler, B.; Conrad, F.; Speldrich, M.; Kögerler, P.; Boskovic, C.; Patzke, G. R. *Dalton Trans.* **2009**, 4423.

(11) Hussain, F.; Patzke, G. R. *CrystEngComm* **2011**, *13*, 530.

(12) Hussain, F.; Gable, R. W.; Speldrich, M.; Kögerler, P.; Boskovic, C. *Chem. Commun.* **2009**, 328.

(13) Ritchie, C.; Moore, E. G.; Speldrich, M.; Kögerler, P.; Boskovic, C. *Angew. Chem., Int. Ed.* **2010**, *49*, 7702.

(14) Ritchie, C.; Speldrich, M.; Gable, R. W.; Sorace, L.; Kögerler, P.; Boskovic, C. *Inorg. Chem.* **2011**, *50*, 7004.

(15) Li, S. Z.; Wang, Y.; Ma, P. T.; Wang, J. P.; Niu, J. Y. *CrystEngComm* **2014**, *16*, 10746.

(16) Wang, Y.; Sun, X. P.; Li, S. Z.; Ma, P. T.; Wang, J. P.; Niu, J. Y. *Dalton Trans.* **2015**, *44*, 733.

(17) Wang, Y.; Sun, X. P.; Li, S. Z.; Ma, P. T.; Niu, J. Y.; Wang, J. P. *Cryst. Growth Des.* **2015**, *15*, 2057.

(18) Shi, D.-Y.; Zhao, J.-W.; Chen, L.-J.; Ma, P.-T.; Wang, J.-P.; Niu, J.-Y. *CrystEngComm* **2012**, *14*, 3108.

(19) Chen, L. J.; Zhang, F.; Ma, X.; Luo, J.; Zhao, J. W. *Dalton Trans.* **2015**, *44*, 12598.

(20) (a) Sheldrick, G. M. *SHELXL97, Program for Crystal Structure Refinement*; University of Göttingen: Göttingen, Germany, 1997. (b) Sheldrick, G. M. *SHELXS97, Program for Crystal Structure Solution*; University of Göttingen: Göttingen, Germany, 1997.

(21) Brown, I. D.; Altermatt, D. *Acta Crystallogr., Sect. B: Struct. Sci.* **1985**, *B41*, 244.

(22) Nellutla, S.; van Tol, J.; Dalal, N. S.; Bi, L.-H.; Kortz, U.; Keita, B.; Nadjo, L.; Khitrov, G. A.; Marshall, A. G. *Inorg. Chem.* **2005**, *44*, 9795.

(23) (a) Tourné, C.; Revel, A.; Tourné, G.; Vendrell, M.; Hebd, C. R. *Seances Acad. Sci. Ser. C* **1973**, *277*, 643. (b) Kortz, U.; Savelieff, M. G.; Bassil, B. S.; Dickman, M. H. *Angew. Chem., Int. Ed.* **2001**, *40*, 3384.

(24) (a) Szeto, K. C.; Lillerud, K. P.; Tilset, M.; Bjørgen, M.; Prestipino, C.; Zecchina, A.; Lamberti, C.; Bordiga, S. *J. Phys. Chem. B* **2006**, *110*, 21509. (b) Bordiga, S.; Damin, A.; Bonino, F.; Zecchina, A.; Spanò, G.; Rivetti, F.; Bolis, V.; Lamberti, C. *J. Phys. Chem. B* **2002**, *106*, 9892. (c) Zhao, J.-W.; Wang, C.-M.; Zhang, J.; Zheng, S.-T.; Yang, G.-Y. *Chem. - Eur. J.* **2008**, *14*, 9223.

(25) Sarma, M.; Chatterjee, T.; Das, S. K. *Dalton Trans.* **2011**, *40*, 2954.

(26) Auwer, C. D.; Charbonnel, M. C.; Drew, M. G. B.; Grigoriev, M.; Hudson, M. J.; Iveson, B. P.; Madic, C.; Nierlich, M.; Presson, M. T.; Revel, R.; Russell, M. L.; Thuery, P. *Inorg. Chem.* **2000**, *39*, 1487.

(27) Bünzli, J-C. G.; Eliseeva, S. V. *Chem. Sci.* **2013**, *4*, 1939.

(28) (a) Qin, C.; Song, X. Z.; Su, S. Q.; Dang, S.; Feng, J.; Song, S. Y.; Hao, Z. M.; Zhang, H. J. *Dalton Trans.* **2012**, *41*, 2399. (b) Huang, L.; Cheng, L.; Wang, S. S.; Fang, W. H.; Yang, G. Y. *Eur. J. Inorg. Chem.* **2013**, *2013*, 1639. (c) Lu, Y.; Li, Y.; Wang, E.; Xu, X.; Ma, Y. *Inorg. Chim. Acta* **2007**, *360*, 2063. (d) Yang, C. Y.; Zhang, L. C.; Wang, Z. J.; Wang, L.; Li, X. H.; Zhu, Z. M. *J. Solid State Chem.* **2012**, *194*, 270. (e) Wang, X.; Li, J.; Tian, A.; Lin, H.; Liu, G.; Hu, H. *Inorg. Chem. Commun.* **2011**, *14*, 103. (f) Du, M.; Li, C.-P.; Chen, M.; Ge, Z.-W.; Wang, X.; Wang, L.; Liu, C.-S. *J. Am. Chem. Soc.* **2014**, *136*, 10906.

(29) (a) Crosswhite, H. M.; Crosswhite, H. *J. Opt. Soc. Am. B* **1984**, *1*, 246. (b) Dieke, G. H. *Spectra and Energy Levels of Rare Earth Ions in Crystals*; Wiley: New York, 1968. (c) Wybourne, B. G. *Spectroscopic Properties of Rare Earths*; Interscience: New York, 1965. (d) Judd, B. R. *Operator Techniques in Atomic Spectroscopy*; McGraw-Hill: New York, 1963. (e) Blasse, G.; Grabmaier, B. C. *Luminescent Materials*; Springer-Verlag: Berlin, 1994. (f) Hüfner, S. *Optical Spectra of Transparent Rare Earth Compounds*; Academic Press: New York, 1978. (g) Liu, G.; Jacquier, B. *Spectroscopic Properties of Rare Earths in Optical Materials*; Springer: Berlin, 2005. (h) Liu, Y.; Tu, D.; Zhu, H.; Chen, X. *Chem. Soc. Rev.* **2013**, *42*, 6924.

(30) Cui, Y. J.; Yue, Y. F.; Qian, G. D.; Chen, B. L. *Chem. Rev.* **2012**, *112*, 1126.

(31) (a) Moore, E. G.; Samuel, A. P. S.; Raymond, K. N. *Acc. Chem. Res.* **2009**, *42*, 542. (b) Bünzli, J.-C. G. *Chem. Rev.* **2010**, *110*, 2729. (c) Sopasis, G. J.; Orfanoudaki, M.; Zarmpas, P.; Philippidis, A.; Siczek, M.; Lis, T.; O'Brien, J. R.; Milios, C. J. *Inorg. Chem.* **2012**, *51*, 1170.

(32) (a) Wang, X. F.; Liu, C. S.; Yu, T. H.; Yan, X. H. *Phys. Chem. Chem. Phys.* **2014**, *16*, 13440. (b) Zhao, J. W.; Li, H. L.; Li, Y. Z.; Li, C. Y.; Wang, Z. L.; Chen, L. J. *Cryst. Growth Des.* **2014**, *14*, 5495. (c) Zhang, S. W.; Wang, K.; Zhang, D. D.; Ma, P. T.; Niu, J. Y.; Wang, J. P. *CrystEngComm* **2012**, *14*, 8677. (d) Kirby, A. F.; Richardson, F. S. *J. Phys. Chem.* **1983**, *87*, 2544. (e) Stouwdam, J. W. F. C.; van Veggel, J. M. *Nano Lett.* **2002**, *2*, 733. (f) Su, Y.; Li, L.; Li, G. *Chem. Mater.* **2008**, *20*, 6060.

(33) (a) Zhang, T. R.; Spitz, C.; Antonietti, M.; Faul, C. F. J. *Chem. - Eur. J.* **2005**, *11*, 1001. (b) Rocha, J.; Carlos, L. D.; Paz, F. A. A.; Ananias, D. *Chem. Soc. Rev.* **2011**, *40*, 926. (c) Malta, O. L.; Carlos, L. D. *Quim. Nova* **2003**, *26*, 889.

DOI: 10.1021/acs.inorgchem.6b00061
Inorg. Chem. 2016, 55, 3881−3893

(34) (a) Shi, F. N.; Meng, J.; Ren, Y. F.; Su, Q. *J. Mater. Chem.* **1997**, *7*, 773. (b) Shen, X.; Yan, B. *J. Mater. Chem. C* **2015**, *3*, 7038.
(35) (a) Meyer, L. V.; Schönfeld, F.; Müller-Buschbaum, K. *Chem. Commun.* **2014**, *50*, 8093. (b) Chorazy, S.; Nakabayashi, K.; Ohkoshi, S.-I.; Sieklucka, B. *Chem. Mater.* **2014**, *26*, 4072.
(36) Xin, M.; Tu, D. T.; Zhu, H. M.; Luo, W. Q.; Liu, Z. H.; Huang, P.; Li, R. F.; Cao, Y. G.; Chen, X. Y. *J. Mater. Chem. C* **2015**, *3*, 7286.
(37) (a) Fu, Z. L.; Xia, W. W.; Li, Q.; Cui, X. Y.; Li, W. H. *CrystEngComm* **2012**, *14*, 4618. (b) Zhang, Y.; Gong, W. T.; Yu, J. J.; Pang, H. C.; Song, Q.; Ning, G. L. *RSC Adv.* **2015**, *5*, 62527. (c) An, Z. B.; Xiao, X. Z.; Yu, J.; Mao, D. S.; Lu, G. Z. *RSC Adv.* **2015**, *5*, 52533. (d) Wu, L.; Zhang, Y.; Gui, M. Y.; Lu, P. Z.; Zhao, L. X.; Tian, S.; Kong, Y. F.; Xu, J. J. *J. Mater. Chem.* **2012**, *22*, 6463. (e) Watras, A.; Dereń, P. J.; Pązik, R. *New J. Chem.* **2014**, *38*, 5058.
(38) (a) Mialane, P.; Lisnard, L.; Mallard, A.; Marrot, J.; Antic-Fidancev, E.; Aschehoug, P.; Vivien, D.; Sécheresse, F. *Inorg. Chem.* **2003**, *42*, 2102. (b) Ritchie, C.; Baslon, V.; Moore, E. G.; Reber, C.; Boskovic, C. *Inorg. Chem.* **2012**, *51*, 1142.
(39) (a) Li, L. L.; Wang, Z. J.; Yang, Z. P.; Guo, Q. L. *Opt. Commun.* **2014**, *332*, 83. (b) Zhou, J.; Xia, Z. G. *J. Mater. Chem. C* **2015**, *3*, 7552.

DOI: 10.1021/acs.inorgchem.6b00061
Inorg. Chem. 2016, 55, 3881−3893